

# Algorithms for Sea Surface Wind Parameter Extraction from X-band Shipborne Nautical Radar Images

by

© Ying Liu, B. Eng.

A thesis submitted to the School of Graduate Studies  
in partial fulfilment of the requirements for the degree of  
Master of Engineering

Department of Electrical and Computer Engineering  
Faculty of Engineering and Applied Science  
Memorial University of Newfoundland

May 2015

St. John's

Newfoundland

## Abstract

In this thesis, research for improving sea surface wind parameter extraction from shipborne X-band marine radar images is presented. First, the curve-fitting-based wind algorithms are investigated. To exclude the rain cases and low-backscatter images, a data quality control process is designed. Then, a dual-curve-fitting technique is proposed to enhance the wind retrieval performance under low sea states. This modified curve-fitting-based wind algorithm is tested using radar images and shipborne anemometer data collected on the east coast of Canada. It is shown that the dual-curve-fitting algorithm produces improvements in the mean differences between the radar and the anemometer results for wind direction and speed of about  $5.7^\circ$  and  $0.3$  m/s, respectively, under sea states with significant wave height lower than  $2.30$  m. Secondly, the intensity-level-selection- (ILS-) based wind algorithms are studied. An additional process is implemented for the ILS-based method to improve the accuracy of wind measurements, including the recognition of blockages and islands in the temporally integrated radar images. Moreover, a harmonic function that is least-squares fitted to the selected range distances vector as a function of antenna look direction is applied. This modified ILS-based wind algorithm is applied to the same radar data. Compared with the original ILS-based algorithm, the modified one reduces the standard deviation (STD) of wind direction and speed by about  $4^\circ$  and  $0.2$  m/s, respectively. Also, the above mentioned two modified methods (dual-curve-fitting-based and modified ILS-based) are compared. Finally, X-band radar signatures of rain cells are elaborately described both in time and frequency domains. It is seen that the rain-contaminated image pixels are more uniformly bright than the wave echoes and radar retrieved wind results are thus overestimated. This property of “uniformly bright” is used to identify the portions that are more affected by rain. To mitigate the effects of rain on wind retrieval from X-band radar images, a novel texture-analysis-based data filtering process is presented and tested. By removing

the data in the directions more affected by rain, significant improvements can be seen from the radar-derived wind results using both of the two wind algorithms.

## Acknowledgements

The author would like to thank the Faculty of Engineering and Applied Science for affording her the opportunity of conducting this work. Particularly, the supervision provided by Dr. Weimin Huang and Dr. Eric W. Gill, and the patience and encouragement that they have shown throughout the research period are greatly appreciated. Their suggestions and insights regarding the topic have been invaluable.

The author is grateful for financial support in the forms of a Natural Sciences and Engineering Research Council of Canada grants to Dr. E. W. Gill (NSERC 238263-10) and Dr. W. Huang (NSERC 402313-12), and an Atlantic Innovation Fund (AIF) to Dr. E. W. Gill.

The author would also like to thank Dr. E. Thornhill of Defence Research and Development Canada (DRDC) for providing the radar and buoy data.

Finally, the author deeply appreciates the understanding and patience of the author's parents, Mr. Zile Liu and Mrs. Jinhua Zeng. This work could not be completed without their support.

# Contents

|  |             |
|--|-------------|
| <b>Abstract</b>  | <b>ii</b>   |
| <b>Acknowledgements</b>                                | <b>iv</b>   |
| <b>List of Tables</b>                                  | <b>viii</b> |
| <b>List of Figures</b>                                 | <b>ix</b>   |
| <b>Table of Acronyms</b>                               | <b>xii</b>  |
| <b>Table of Symbols</b>                                | <b>xiv</b>  |
| <b>1 Introduction</b>                                  | <b>1</b>    |
| 1.1 Research Rationale . . . . .                       | 1           |
| 1.2 Literature Review . . . . .                        | 3           |
| 1.3 The Organization and Scope of the Thesis . . . . . | 11          |
| <b>2 Curve-fitting-based Wind Algorithms</b>           | <b>12</b>   |
| 2.1 Original Curve-fitting-based Algorithm . . . . .   | 13          |
| 2.1.1 Rain recognition . . . . .                       | 13          |
| 2.1.2 Wind Direction . . . . .                         | 15          |
| 2.1.3 Wind Speed . . . . .                             | 16          |
| 2.2 Modified Curve-fitting-based Algorithm . . . . .   | 17          |

|          |  |           |
|----------|--|-----------|
| 2.2.1    | Low-backscatter Image Recognition . . . . .                                      | 17        |
| 2.2.2    | Dual-curve-fitting . . . . .   | 17        |
| 2.3      | Results . . . . .  | 19        |
| 2.4      | General Chapter Summary . . . . .  | 23        |
| <b>3</b> | <b>ILS-based Wind Algorithms</b>   | <b>25</b> |
| 3.1      | Original ILS-based Algorithm . . . . .   | 26        |
| 3.1.1    | Temporal Integration and Smoothing . . . . .                                     | 26        |
| 3.1.2    | Intensity-level-selection . . . . .  | 26        |
| 3.1.3    | Wind Direction . . . . .   | 28        |
| 3.1.4    | Wind Speed . . . . .   | 29        |
| 3.2      | Modified ILS-based Method . . . . .  | 30        |
| 3.2.1    | Blockage Recognition . . . . .   | 30        |
| 3.2.2    | Curve-fitting . . . . .  | 30        |
| 3.2.3    | Island Recognition . . . . .   | 31        |
| 3.3      | Results . . . . .  | 32        |
| 3.3.1    | Original ILS vs. Modified ILS . . . . .  | 33        |
| 3.3.2    | Dual-curve-fitting vs. Modified ILS . . . . .                                    | 36        |
| 3.4      | General Chapter Summary . . . . .  | 39        |
| <b>4</b> | <b>Wind Parameter Extraction from Rain-contaminated Radar Data</b>               | <b>40</b> |
| 4.1      | The Effects of Rain . . . . .  | 41        |
| 4.1.1    | On Radar Intensity Images . . . . .  | 41        |
| 4.1.2    | On Radar Image Spectra . . . . .   | 42        |
| 4.1.3    | On Wind Parameters Extraction . . . . .  | 42        |
| 4.2      | Detailed Methodology for Wind Algorithms Incorporating Rain Mitigation . . . . . | 45        |
| 4.2.1    | Texture Analysis . . . . .   | 45        |

|          |  |           |
|----------|--|-----------|
| 4.2.2    | Data Filtering . . . . .                           | 47        |
| 4.2.3    | Wind Direction . . . . .                           | 49        |
| 4.2.4    | Wind Speed Model Correction . . . . .              | 51        |
| 4.3      | Results . . . . .                                  | 52        |
| 4.4      | General Chapter Summary . . . . .                  | 54        |
| <b>5</b> | <b>Conclusions</b>                                 | <b>57</b> |
| 5.1      | General Synopsis and Significant Results . . . . . | 57        |
| 5.2      | Suggestions for Future Work . . . . .              | 58        |
|          | <b>Bibliography</b>                                | <b>60</b> |

# List of Tables

|     |   |    |
|-----|---|----|
| 2.1 | Data Information . . . . .  | 20 |
| 2.2 | Wind speed and direction error statistics: bias and STD . . . . .     | 21 |
| 3.1 | Wind speed and direction error statistics: bias and STD . . . . .     | 33 |
| 4.1 | Wind speed and direction error statistics from rain-contaminated data | 53 |

# List of Figures

|     |  |    |
|-----|--|----|
| 1.1 | Illustration of Bragg scattering. . . . .  | 5  |
| 1.2 | Block diagram of WaMoS. . . . .  | 7  |
| 1.3 | An example of a real-time X-band marine radar image based on WaMoS. . . . .  | 8  |
| 2.1 | Example of images (left) and their histograms (right): (a) a normal case; (b) a rain-contaminated case; (c) a low-backscatter case. . . . .  | 14 |
| 2.2 | Range-averaged radar backscatter grey scale intensity as a function of antenna look direction for an image collected at 03:03, Nov. 29, 2008. . . . .  | 15 |
| 2.3 | Scatter plot showing the wind speed from anemometer, corresponding radar backscatter intensity, and the best-fit curve based on a third order polynomial function for Decca data acquired during Nov. 28-29, 2008. . . . .   | 16 |
| 2.4 | Example of the Decca radar data from Dataset 1 (collected at 02:22, Nov. 29, 2008): (a) backscatter image; (b) range-averaged backscatter intensity as a function of antenna look direction using single-curve-fitting; (c) range averaged backscatter intensity as a function of antenna look direction using dual-curve-fitting. . . . . | 18 |
| 2.5 | Comparison of wind results using Dataset 3 (Decca) from 01:12 to 05:31, Nov. 29, 2008: (a) wind direction; (b) wind speed; (c) significant wave height and percentage of directions with many low intensity pixels; (d) ship speed and ship direction. . . . .   | 22 |

|     |   |    |
|-----|---|----|
| 3.1 | Block diagram of the original ILS-based wind algorithm. . . . .   | 27 |
| 3.2 | An integrated radar image without blockage. . . . .   | 28 |
| 3.3 | Conversion function model obtained using Dataset 2 (Furuno). . . . .  | 29 |
| 3.4 | A blockage case: (a) an integrated image with blockage; (b) the selected range distances vector referred to (a) before curve-fitting; (c) the selected range distances vector referred to (a) after curve-fitting. . . . .      | 31 |
| 3.5 | Illustration of island recognition using Dataset 4 (Furuno): (a) range distances vector (pink line) without island recognition; (b) range distances vector with island recognition; (c) map with ship's track. . . . .          | 32 |
| 3.6 | Comparison results obtained from Dataset 4 (Furuno) with appearance of island: (a) wind direction; (b) wind speed. . . . .  | 34 |
| 3.7 | Comparison of wind results using ILS and modified ILS-based algorithms for Dataset 2: (a) wind direction; (b) wind speed; (c) low-clutter direction percentage; (d) ship speed and ship direction. . . . .                      | 35 |
| 3.8 | Comparison results using dual-curve-fitting and modified ILS-based algorithms for Dataset 1: (a) wind speed; (b) wind direction; (c) low-clutter direction percentage; (d) zero pixel percentage; (e) ship information. . . . . | 37 |
| 4.1 | Examples of marine radar images: (a) single image without rain; (b) single image with rain; (c) integrated image without rain; (d) integrated image with rain. . . . .  | 41 |
| 4.2 | 2-D image spectrum: (a) in the absence of rain; (b) in the presence of rain. . . . .  | 43 |
| 4.3 | Wind field extraction comparison results using ILS based algorithms with and without rain: (a) wind speed; (b) wind direction; (c) zero pixel percentage. . . . .   | 44 |

|      |  |    |
|------|--|----|
| 4.4  | Examples of marine radar images and the their texture maps: (a) rain-free radar backscatter intensity image; (b) rain-contaminated radar backscatter intensity image; (c) rain-free texture map of (a); (d) rain-contaminated texture map (b). . . . .                             | 46 |
| 4.5  | Block diagram of rain mitigation. . . . .  | 48 |
| 4.6  | Number of data points $N_\phi$ of: (a) rain-free original image; (b) rain contaminated original image; (c) rain-free texture map; (d) rain-contaminated texture map. . . . .   | 49 |
| 4.7  | Illustration of rain mitigation incorporated curve-fitting based algorithms: (a) the original radar image; (b) the texture map; (c) curve-fitting based method without rain mitigation; (d) curve-fitting based method with rain mitigation. . . . .                               | 50 |
| 4.8  | Illustration of rain mitigation incorporated ILS based algorithms: (a) ILS without rain mitigation; (b) ILS with rain mitigation; (c) modified ILS-based method without rain mitigation; (d) modified ILS-based method with rain mitigation. . . . .                               | 51 |
| 4.9  | Training models: (a) curve-fitting-based wind speed model from rain-free data; (b) curve-fitting-based wind speed model from rain-contaminated data; (c) ILS-based conversion function from rain-free data; (d) ILS-based conversion function from rain-contaminated data. . . . . | 52 |
| 4.10 | Wind results from rain-contaminated data using the curve-fitting based algorithms: (a) wind speed; (b) wind direction; (c) rain rejection percentage; (d) ZPP and precipitation. . . . .   | 55 |
| 4.11 | Wind results from rain-contaminated data using the ILS based algorithms: (a) wind speed; (b) wind direction; (c) rain rejection percentage; (d) ZPP and precipitation. . . . .   | 56 |

# List of Acronyms

The page numbers here indicate the place of first significant reference.

- ILS : Intensity Level Selection (p. ii).
- STD : Standard Deviation (p. ii).
- DRDC : Defence Research and Development Canada (p. iv).
- SAR : Synthetic-Aperture Radar (p. 2).
- LIDAR : Airborne Scanning Light Detection and Ranging  
(p. 2).
- GNSS-R : Global Navigation Satellite System-Reflectometry  
(p. 2).
- HF : High-Frequency (p. 2).
- HH : Horizontal polarization on transmitter and receiver  
(p. 3).
- WaMoS : Wave Monitoring System (p. 6).
- GKSS : Helmholtz-Zentrum Geesthacht (currently re-named)(p. 6).

PC : Personal computer (p. 6).

NRCS : Normalized Radar Cross-Section (p. 6).

GMF: Geophysical Model Function (p. 9).

ZPP : Zero Pixel Percentage (p. 13).

LCDP : Low-Clutter Direction Percentage (p. 17).

SNR : Signal-to-Noise Ratio (p. 19).

CFAV : Canadian Forces Auxiliary Vessel (p. 20).

RPM : Revolutions Per Minute (p. 20).

CPU : Central Processing Unit (p. 38).

FFT : Fast Fourier Transform (p. 42).

RRP : Rain Rejection Percentage (p. 48).

# Table of Symbols

The page numbers here indicate the place of first significant reference. Although not all symbols are explicitly referenced below, their definitions are obvious from the context.

- $L$  : Spacing between scatterers (p. 4).
- $\theta$  : Incidence angle (p. 4).
- $\lambda$  : Wavelength of the radio waves (p. 4).
- $\lambda_w$  : Wavelength of the water waves (p. 5).
- $Ri_b$  : Richardson number (p. 7).
- $g$  : Gravitational acceleration of Earth (p. 7).
- $x, y$  : Axis of the coordinates of the horizontal sea level plane (p. 7).
- $z$  : Height above the sea level (p. 7).
- $P_v$  : Virtual potential temperature (p. 7).
- $P_0$  : Surface Potential temperature (p. 7).
- $u$  : Wind velocity component in the  $x$ - direction (p. 7).
- $v$  : Wind velocity component in the  $y$ - direction (p. 7).

- $Z_T$ : Threshold of ZPP for rain recognition (p. 13).
- $\phi$ : Antenna look direction (p. 15).
- $\sigma_\phi$ : Range-averaged radar backscatter grey scale intensity (p. 15).
- $a_0, a_1, a_2$ : Regression parameters for the curve-fitted range-averaged intensity (p. 15).
- $\sigma_{wSpd}$ : Overall averaged radar backscatter intensity (p. 16).
- $I_i$ : Temporally integrated radar image (p. 26).
- $L_i$ : Intensity level of the integrated image  $I_i$  (p. 27).
- $r_i$ : Range distances vector of the integrated image  $I_i$  (p. 27).
- $r_i^s$ : Smoothed range distances vector of  $r_i$  (p. 27).
- $u_0$ : Wind speed (p. 29).
- $\phi_0$ : Wind direction (p. 29).
- $\alpha_i$ : Conversion rate for integrated image  $I_i$  (p. 29).
- $\beta_j$ : Regression parameters for the conversion rate  $\alpha_i$  (p. 29).
- $b_0, b_1, b_2$ : Regression parameters for the smoothed range distances vector  $r_i^s$  (p. 31).
- $I_{p,q}$ : Radar backscatter intensity of the pixel  $(p, q)$  (p. 45).

- $T(I_{p,q})$ : Texture of the pixel intensity  $I_{p,q}$  (p. 45).
- $I_T$ : Threshold of the pixel intensity in an azimuthal direction (p. 47).
- $N_\phi$ : Number of data points of the pixels whose intensities are less than  $I_T$  in each azimuthal direction (p. 47).
- $N_T$ : Threshold of  $N_\phi$  for recognizing more-affected portions by rain (p. 47).

# Chapter 1

## Introduction

This chapter explains why X-band radars are chosen to measure sea surface wind vectors instead of other sensors. Then, the literature about the current applicable wind algorithms is summarized. Also, the literature about the effects of rain on the radar images is investigated. Finally, the scope of this thesis is outlined.

### 1.1 Research Rationale

Wind information is important for studying energy exchange processes between the atmosphere and the ocean surface. Also, sea surface wind measurements play a significant role in marine navigation and safety. Currently, shipborne anemometers are the most common *in-situ* wind measurement tools and have been widely installed for those purposes. However, anemometer measurements may be negatively impacted by a ship's motion and structure. Even for anemometers at a well-exposed location, wind speed measurements may have an error of up to 10% [1]. This is one of the main reasons why efforts are now being made to recover wind information from other sensors. Compared to a traditional *in-situ* anemometer that provides point measurements, remote sensing technology offers a possibility to measure wind over a relatively large sea surface area using only one set of instruments.

Currently, remote sensing equipment can be categorized in terms of platforms: land-based, air-based and space-based sensors that use either an active or passive source [2]. Each classification has its own expense, adaptability, and resolution as well as spatial and temporal coverage. Space-based systems usually possess large spatial coverage. For example, the widely used satellite-borne Synthetic Aperture Radar (SAR) and airborne-scanning Light Detection and Ranging (LIDAR) systems are able to achieve large-area coverage. In addition, LIDAR may be used to obtain 3-D wind information. However, this type of sensor often costs more because of its relatively complex instrumentation. More recently, some simpler space-based sensors came into being, for instance the Global Navigation Satellite System Reflectometry (GNSS-R) [3]. However, for space-based systems, the revisit time (elapsed time between observations of the same point on earth) is on the order of days, and thus wind cannot be measured at an arbitrarily specified moment. On the other hand, land-based radars may have a larger temporal coverage; e.g., X-band marine radars are capable of monitoring oceanic and atmospheric parameters over the course of seconds [4]. In this way, X-band marine radars hold the potential to recover wind information in real-time, and this advantage largely compensates for their relatively limited spatial coverage. Meanwhile, high frequency (HF) land-based radars, which are mainly used for large area currents, wind and wave measurements, provide a compromise between spatial and temporal coverage. HF radars also require significant expenses and they are generally too large to be installed on vessels. As a result, the shipborne X-band marine radars, widely available in the market have become a good choice, given that they provide an accurate, real-time, and cost-efficient shipborne sea surface wind retrieval for navigation. X-band marine radars can illuminate a sea surface area (with a radius up to 30 km) continuously in space and time with high resolution, and may operate automatically from moving vessels and coastal sites [5]. Typical remote sensing parameters obtained using this type of sensor include essential wave

information such as wave height and period [6]–[7], sea surface current velocities [8]–[11], wind vectors [12]–[17], and shallow water bathymetry [18]–[20].

This research concentrates on sea surface wind information on which many onshore and offshore operations are critically dependent. For example, in order to finance wind farm projects, collection of wind speed and direction data is crucial for determining site potential [21]. Local winds monitored by shipborne X-band marine radars can provide more detailed data with high efficiency for accurate siting. Also, routine sea surface wind measurements surrounding a moving vessel are required to enhance navigation security. In this context, compared to traditional anemometers, wind measurements using X-band marine radar may have an advantage in that they are independent of the sensor’s installation height and motion [4]. Such radars are also useful for obtaining wind parameters used in determining the influence of ocean winds on the ecosystem in upwelling regions [22]. In view of these possible advantages and applications, this research focuses on the sea surface wind field retrieval using shipborne X-band radar.

## 1.2 Literature Review

Marine X-band radar systems operating at grazing incidence are widely used on ships for navigation. Since standard marine radars are non-coherent and operate with horizontal polarization in transmitter and receiver modes (i.e., HH polarization), coherent and vertical polarized radars will not be discussed in this research. To obtain wind and wave information from the radar backscatter images, a better understanding of the imaging mechanism is required.

At grazing incidence angles, specular reflection is the dominant process, but the radar backscattering mechanism is not very well understood. In the 1970s, Barrick [23]–[25] and Bass *et al.* [26] pioneered scattering theories for the sea surface.

The concept was introduced that the temporally and spatially changing sea surface can be considered as being made up of a large number of small facets oriented at different angles. Calculating the scattered electromagnetic energy from all the facets is a very intricate boundary value problem [27]. This has led to significant efforts being expended on approximate scattering methods to yield both quantitative predictions and physical insight [28]. The quasi-specular approximation is one of the notable scattering methods. This approximation method can be used to predict the average scattering from sea surface in a specific direction and for a certain range [29]. Barrick [25] discussed the wind dependence of quasi-specular microwave sea scatter. It was shown that a specular-point scattering model adequately describes the relation between the average quasi-specular microwave scattering cross-section of the sea surface and the mean wind speed. In 1990, Brown summarized and developed the quasi-specular approximation and a good overview was given in [28].

Scattering from the ocean surface at grazing angles is not only dependent on quasi-specular scattering which relies on large scale ocean waves, but it is also subject to effects produced by the small-scale surface waves. It is generally accepted that the most important mechanism contributing to the interaction between radar and ocean surface waves is Bragg scattering [27]. In the original theory, crystal lattices were designed as an array of isolated scatterers, and Bragg [30] found in 1913 that if the round trip distance between consecutive scatterers is equal to an exact number of the electromagnetic wavelengths, the radio waves reinforce each other. This finding can be referred to as Bragg diffraction, or resonance. In 1955, Bragg resonance resulting from radar signals interacting with ocean waves was first discussed by Crombie [31]. He found that the strongest backscatter from the ocean waves occurred at grazing incidence where the ocean wavelength was exactly one half of the incident radio wavelength (see Fig. 1.1). The Bragg condition in general is given by [30]

$$\frac{2L \sin \theta}{\lambda} = n \quad n = 1, 2, \dots \quad (1.1)$$

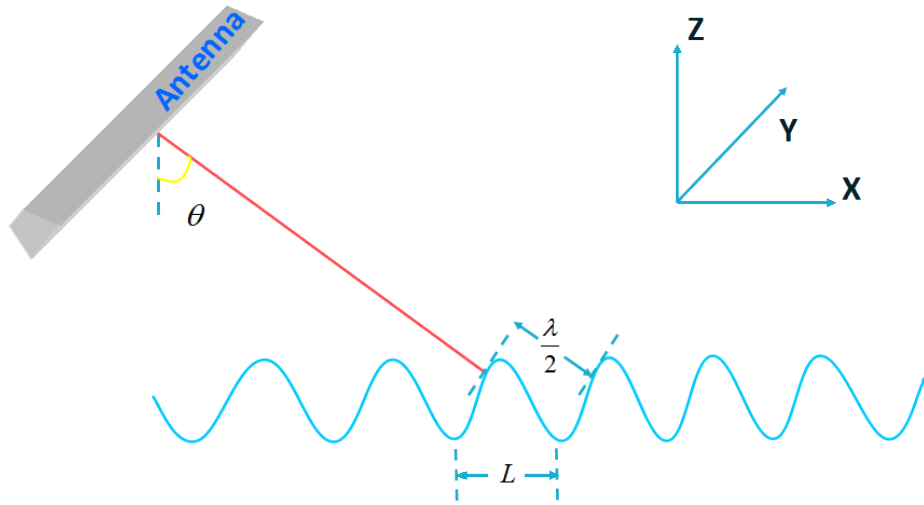


Figure 1.1: Illustration of Bragg scattering.

where  $L$  is the spacing between scatterers,  $\theta$  represents the incidence angle, and  $\lambda$  is the radio wavelength. In 1966, a laboratory experiment for X-band radar performed by Wright [32] indicated that the backscatter from water waves agrees well with the Bragg scattering theory. Therefore, the radar backscatter from the sea surface is governed by Bragg-selected waves of the wavelength

$$\lambda_w = \frac{n\lambda}{2 \sin \theta}. \quad (1.2)$$

In 1968, a composite surface theory was proposed by Bass *et al.* [26] and Wright [33]. It was assumed that: i) the large scale ocean surface is approximated by an array of facets. Each of the facets is tilted by the long waves; ii) the small-scale ocean surface waves (capillary waves) are modulated by long waves. Bragg theory is applied to each small facet, and the net radar backscatter can thus be obtained by summing over the contribution from all facets [4]. In 1990, Plant [34] extended discussion of Bragg and composite surface theories from the air/sea interface, and Wetzel [35] provided a review of the physics of grazing incidence radar backscatter. It was found that the frequency, incidence angle, and polarization dependence of the

sea echo at microwave frequencies can be well explained by the Bragg theory. For a HH-polarized X-band marine radar operating at 9.41 GHz (i.e., a wavelength of 3 cm) and grazing angles, cm-scale surface capillary waves which are modulated by the ocean waves are responsible for the backscatter. This provides an explanation for why sea surface waves can be imaged by a radar. Meanwhile, tilt modulation and hydrodynamic modulation are well established imaging mechanisms at moderate incidence angles [36]–[38]. Moreover, shadowing effects occur when the incidence angle is greater than the slope angle of the ocean waves, and parts of the sea surface are masked from the radar’s field of view [39]. While Bragg scattering remains important at grazing incidence, shadowing is assumed to be one of the main modulation mechanisms as well [40]. A comprehensive overview of radar backscattering mechanisms was given by Robinson [41]. In the 1980s, the displayed nautical radar images were recorded on photographic film and then digitized using an image processor, which is time-consuming and needs frequent maintenance. Also, most information about the backscatter intensity may be lost with the conventional black and white image display [42]. In order to realize real-time radar-based wind and wave measurements, a combined hard- and software system called WaMoS (Wave Monitoring System) was developed in 1995 at the GKSS research centre (Helmholtz-Zentrum Geesthacht, currently) [43]. This system consists of a standard marine radar, a radar display unit, an analog-to-digital (A/D) converter and a personal computer (PC) for data storage and analysis [5] (see Fig. 1.2). Given a high radiometric resolution, WaMoS can provide efficient, accurate, and real-time sea surface images (see Fig. 1.3) [4]. This research is based on radar data provided by WaMoS and focuses on real-time sea surface real-time wind retrieval.

Having developed a knowledge of the imaging mechanism, further investigations are necessary in order to clarify why nautical X-band radar can be used to measure wind information. Nautical X-band radar backscatter from the ocean surface is mainly

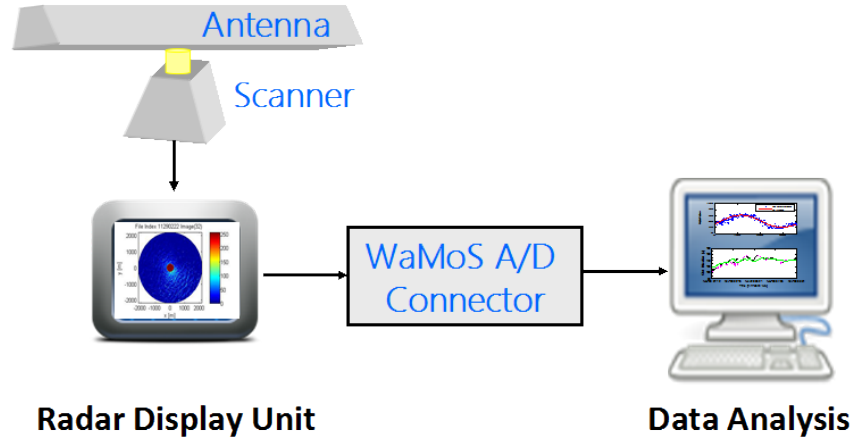


Figure 1.2: Block diagram of WaMoS.

due to its interaction with the small-scale roughness which is controlled by local wind [44]–[48]. It has been shown that the normalized radar cross section (NRCS) strongly depends on wind speed [45], [49]–[50], direction [47], [49], and range to the radar. For HH-polarized radiation at grazing incidence, the NRCS has only one peak in the upwind direction [47], [49]. The single peak in upwind direction may result from the scattering due to small scale breaking waves [48]. Also, it was found that the backscatter intensity can be related to the wind speed [51], and an exponential function for wind speed retrieval was successfully utilized in [12]–[13]. These dependencies on wind direction and speed are the basis of the wind algorithms investigated in this research. Moreover, radar backscatter intensity may be influenced by the physical environments in the boundary layer between the ocean and lower atmosphere—for example, stratification conditions induced by air-sea temperature differences [15]. It is revealed in [52] that unstable stratification conditions may result in higher radar backscatter intensity, thereby affecting wind retrieval. A simple measure of the boundary layer stability is given by the bulk Richardson number  $Ri_b$  [15]

$$Ri_b = \frac{gz(P_v - P_0)}{P_v(u^2 + v^2)}, \quad (1.3)$$

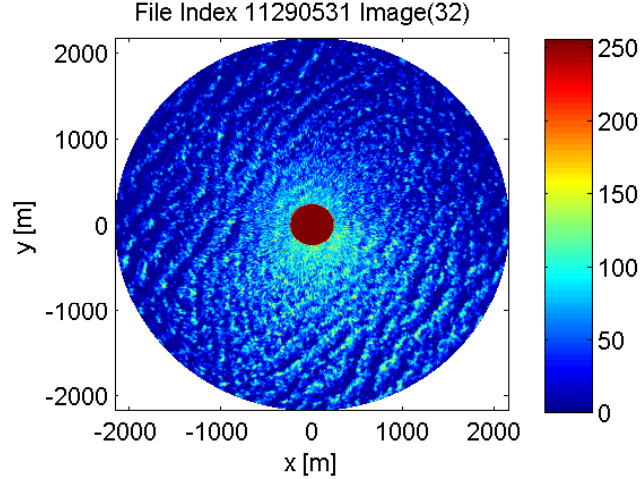


Figure 1.3: An example of a real-time X-band marine radar image based on WaMoS.

where  $P_v$  is the virtual potential temperature,  $P_0$  is the potential surface temperature,  $x$ - and  $y$ - represent the axis of the coordinates of the horizontal sea level plane.  $u$  and  $v$  are the wind components in the  $x$ - and  $y$ -direction, respectively,  $g$  is the acceleration due to gravity, and  $z$  is the height above sea level [53]. If  $Ri_b$  approaches zero, the boundary layer tends to be neutral. Here, it is presumed that air-water temperature differences  $P_v - P_0$  are small, and wind speeds  $u$  and  $v$  are relatively high. Thus,  $Ri_b$  is close to zero and a stable boundary layer can be assumed. For the analysis presented in this thesis, the influence of the stratification conditions will be neglected. In summary, the dependence of the NRCS on wind direction and wind speed, as well as the assumption of a stable boundary layer, lays the foundation of wind parameter recovery using X-band marine radars.

Next, literature about how wind information is extracted from nautical X-band marine radar images is reviewed. During the mid 1980s to the late 1990s, the strong dependence of X-band radar return from the sea surface on both wind direction and speed were continuously validated [44], [46]. Among the first to derive sea surface wind parameters from nautical X-band radar images were Dankert *et al.* [12] - [14]. In 2003, they first determined wind direction from quasi-stationary wind streaks, and extracted wind speed from the temporally integrated radar images and the retrieved

wind direction. However, this approach requires an additional processing step in order to be applied to shipborne radar data because, as a result of the platform's horizontal motion, wind streaks are difficult to extract [16]. Also, a 180° directional ambiguity exists in the wind direction results but it can be removed by extracting the movement of wind gusts visible in the radar image sequence [13].

Most recently, to overcome the previously existing limitations, both Lund *et al.* [15] and Vicen-Bueno *et al.* [17] developed methods which are independent of platform movement. In 2012, by utilizing the radar backscatter intensity dependence on the upwind direction, Lund *et al.* [15] proposed a least-squares curve-fitting technique to identify the upwind peak and an empirical third-order polynomial to calculate wind speed. In 2013, Vicen-Bueno *et al.* [17] developed an effective backscatter intensity-level-selection (ILS) algorithm based on temporal integration and spatial smoothing as well as an empirical third-order polynomial geophysical model function (GMF) to derive wind direction and speed. The latter two algorithms can be applied to radar data collected from a moving ship, and thus are considered in this research. However, modifications need to be made for these two algorithms. In the curve-fitting process, although the data in the directions due to blockage were excluded, the low-intensity data in many azimuthal directions due to low sea states rather than the obstruction by ship structures may be retained, and the result becomes less accurate. Under these circumstances, a second stage of curve-fitting is proposed to reduce the wind estimation error. On the other hand, since the obstruction of the radar field of view or appearance of islands was not considered in [17], an additional process for recognizing the view of blockages and islands as well as a similar curve-fitting technique are designed for the ILS-based algorithm.

A remaining complex challenge involves the negative impact which rain contamination of the marine radar data may have on the extraction of wind and wave parameters [15], [54]. It has been observed that rain affects the radar backscatter through

volume scattering and attenuation by raindrops in the intervening atmosphere and by sea surface roughness changes caused by rain impinging on the ocean [55], [56]. Whether the NRCS is increased or decreased by rain depends on rain rate, raindrop size, radar frequency and polarization [54]–[56]. Raindrops impinging on the sea surface generate ring waves which enhance the sea surface roughness and generate upper-water-layer turbulence which attenuates the short surface wave [57]. In areas of heavy rain, the X- (8.2 to 12.4 GHz) and C-band (4 to 8 GHz) NRCS is usually enhanced, while the L-band (1 to 2 GHz) NRCS is reduced [54].

From shipborne X-band marine radar images, it has been observed that sea surface radar backscatter intensity in the presence of rain is significantly enhanced [15], [58]. Radar backscatter becomes more uniformly bright, particularly at medium ranges [15] and downwind directions [59]. Lund *et al.* [15] proposed a technique to recognize the rain-contaminated images as a novel data quality control procedure. However, those images were then discarded from the wind retrieval analysis. In [15], [58], it turned out that: i) the retrieved wind speed was overestimated in the presence of rain, compared to the results obtained from rain-contamination-free data; ii) due to the impinging effects of rain and rain-related wind effects, wind direction results were obtained less robustly. These findings agree with the NRCS analysis in [54]. Thus, further improvement in wind estimation from data containing rain signatures is desirable.

Although attempts, which might be applied at X-band, have been made to build wind/rain backscatter models at C-band [60] and Ku-band (12 to 18 GHz) [56], the effects of rain on wind parameter extraction from X-band marine radar images still need to be addressed. For marine radars whose primary use is target detection, filters have been designed and rain clutter control circuits have been installed to suppress rain clutter [61]. In [62], a texture-analysis-based fuzzy logic filter for removing echoes (e.g., ground clutter) from rainfall accumulation maps of polarimetric radars was proposed to improve rain rate estimation. The texture here can be interpreted as a

measure of the spatial variance. Inspired by this concept, spatial-variability analysis was exploited in [58] to recognize the characteristics of being “more uniformly bright” in the radar images. Based on the work in [58], [62], a similar texture analysis is applied to the radar images in this research to recognize and remove the more-rain-affected portions of images. This data filtering process can be implemented in the aforementioned wind algorithms to mitigate the effects of rain on wind retrieval. Based on this, a method for wind field estimation from rain-contaminated radar images is proposed here.

### **1.3 The Organization and Scope of the Thesis**

The thesis is organized as follows:

In Chapter 2, a detailed curve-fitting-based methodology and algorithms for wind parameter extraction from shipborne nautical X-band radar data are presented. First, to exclude the cases of rain and low-backscatter images, a data quality control process is designed. Moreover, a dual-curve-fitting is proposed for low sea state conditions and is tested using radar images and shipborne anemometer data.

Chapter 3 details an ILS-based method and the corresponding modifications. The modified ILS-based method includes the recognition of blockages and islands, as well as a harmonic function that is least-squares fitted to the selected range distances vector, from which wind direction can be determined. The performance of the two modified methods (dual-curve-fitting and the modified ILS-based) are compared.

Chapter 4 contains a discussion of the effects of rain on the X-band marine radar images. A texture-analysis-incorporated method for wind parameter extraction from rain-contaminated radar images is proposed and validated.

In Chapter 5, the main conclusions from the previous three chapters are summarized. A few suggestions for future work are also provided.

## Chapter 2

# Curve-fitting-based Wind Algorithms

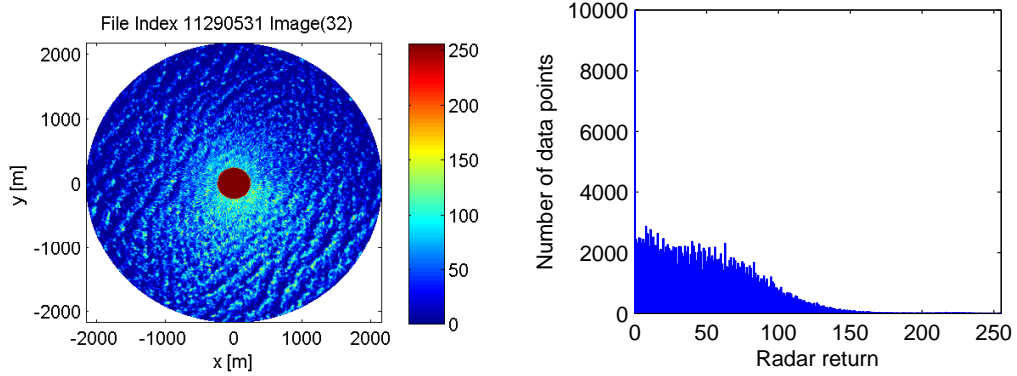
In this chapter, the original curve-fitting-based algorithm [15] for extracting wind parameters from shipborne nautical X-band radar images is introduced. Next, to improve the accuracy of wind retrieval under low sea states, a modified technique, which involves a dual-curve-fitting approach, is proposed. Finally, the modified method is applied to Decca and Furuno radar data collected by DRDC and the results are compared with those obtained from the original curve-fitting-based algorithm and ship-based anemometer data.

## 2.1 Original Curve-fitting-based Algorithm

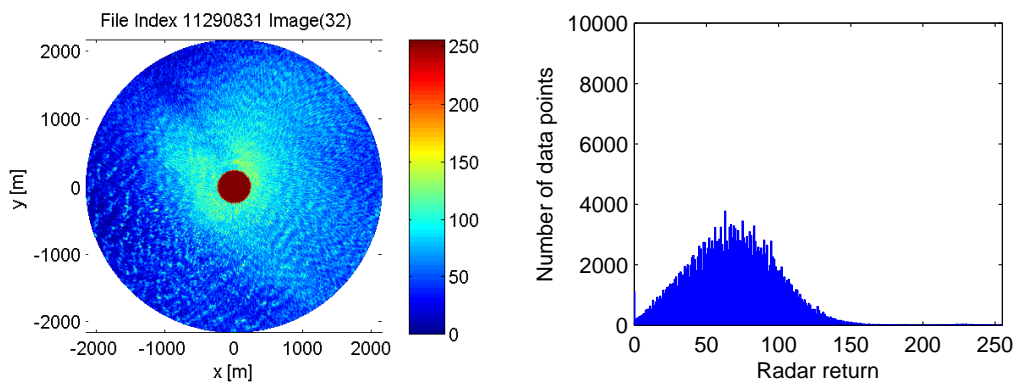
The original curve-fitting-based wind algorithm includes the following steps: i) the radar images are required to go through a rain recognition process; ii) a cosine function that is least-squares fitted to the radar backscatter intensity is used to determine the wind direction (i.e., single-curve-fitting); and iii) an empirical third-order polynomial model is constructed to obtain wind speed from the calculated average intensity value.

### 2.1.1 Rain recognition

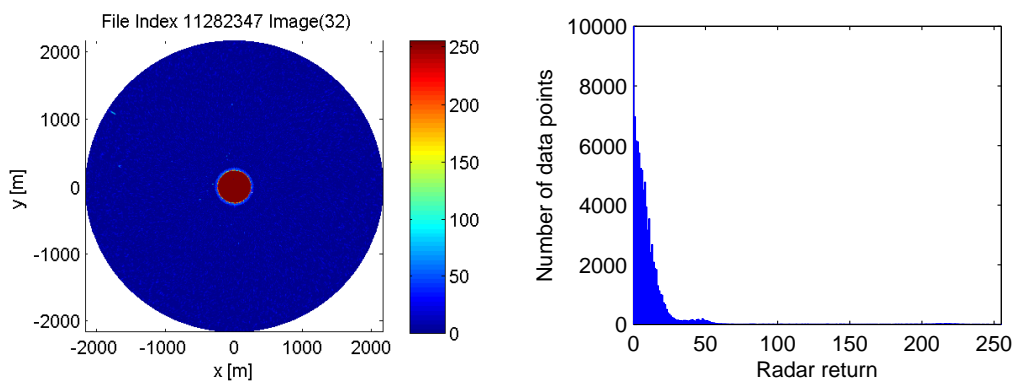
Before using the radar data to retrieve the upwind direction, rain recognition was undertaken for each image by analyzing the radar backscatter intensity histograms. According to [15], due to the strong impact of rain on the number of pixels with zero intensity, the zero-pixel percentage (ZPP, i.e., ratio of the number of image pixels with zero intensity to the overall number of pixels) was identified as a quality control parameter to determine the presence of rain. For the data presented in this thesis, pixels with grey scale intensity lower than 5 were considered as zero-intensity. This value should be adjusted for data with a different grey scale depth. It is worth mentioning that the blockage portion in the images should be excluded for the ZPP calculation. Moreover, it should be noted that the thresholds ( $Z_T$ ) of the ZPP for recognizing rain cases for different radars are different. The difference may be explained by the possibly diverse shadowing effects due to different antenna heights. For Decca radar images, when the ZPP of an image was below 10%, that image was regarded as being contaminated by rain and was excluded from the process of establishing the third-order polynomial model functions of wind speed. For Furuno radar images, which include more blockage portions,  $Z_T$  is 20%. Examples of the corresponding radar backscatter images and their histograms in the absence and presence of rain are shown in Figs. 2.1(a) and (b), respectively. In Fig. 2.1(b), the radar image



(a)



(b)



(c)

Figure 2.1: Example of images (left) and their histograms (right): (a) a normal case; (b) a rain-contaminated case; (c) a low-backscatter case.

looks uniformly bright and the wave signature is blurred, which indicates that rain is probably present, and, for that image, the ZPP is far below 10% .

### 2.1.2 Wind Direction

For HH-polarized X-band radars operating at grazing incidence, it is known that the radar backscatter intensity has only one peak in the upwind direction [47], [49], but a second peak appears in the downwind direction at moderate incidence angles [63]–[64]. To obtain the specific dependence on antenna look direction, radar data for the Decca and Furuno systems used here are averaged over ranges of 450 m to 1500 m and 375 m to 975 m, respectively, for each azimuthal direction. The data are then curve fitted using a cosine square function to give the range-averaged radar backscatter grey scale intensity  $\sigma_\phi$  as [15]

$$\sigma_\phi = a_0 + a_1 \cos^2(0.5(\phi - a_2)) \quad (2.1)$$

where  $a_0$ ,  $a_1$ , and  $a_2$  are the regression parameters. Here,  $\sigma_\phi$  is a function of antenna

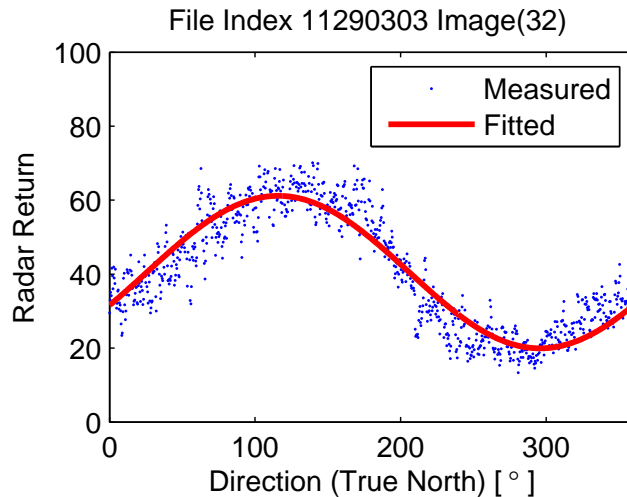


Figure 2.2: Range-averaged radar backscatter grey scale intensity as a function of antenna look direction for an image collected at 03:03, Nov. 29, 2008.

look direction  $\phi$ . An example of curve-fitting is shown in Fig. 2.2. The best-fit curve is shown in red. For each individual radar image, the wind direction can be retrieved from the upwind backscatter peak by using the model-function, Eq. (2.1). The upwind peak direction is given by the regression parameter  $a_2$ . This corresponds to the peak of the best-fit curve, as discussed in [15]. This method works well even when some sections of the radar field of view are masked.

### 2.1.3 Wind Speed

Based on the radar backscatter intensity dependence on wind speed, an empirical third-order polynomial can be derived using the average radar backscatter intensity and the reference wind speed. Then, radar wind speed results can be retrieved from the average intensity value. The overall averaged radar backscatter intensity is calculated as [15]

$$\sigma_{wSpd} = \frac{1}{2\pi} \int_0^{2\pi} (a_0 + a_1 \cos^2(0.5(\phi - a_2))) d\phi, \quad (2.2)$$

Fig. 2.3 shows a scatter plot of the anemometer-measured wind speed and the corre-

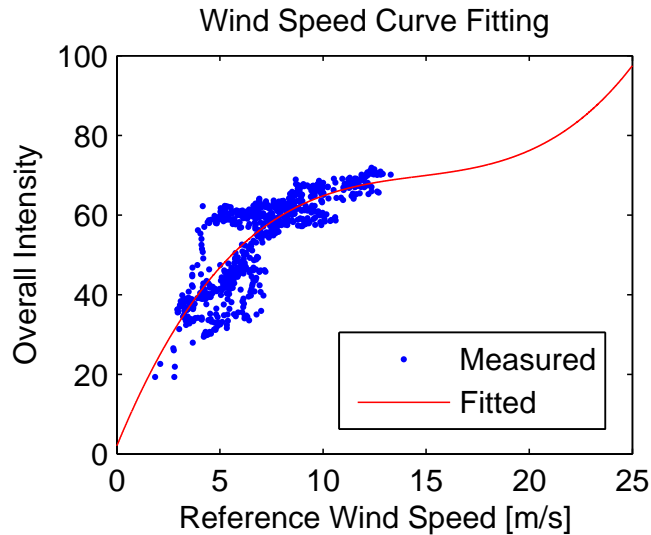


Figure 2.3: Scatter plot showing the wind speed from anemometer, corresponding radar backscatter intensity, and the best-fit curve based on a third order polynomial function for Decca data acquired during Nov. 28-29, 2008.

sponding radar average backscatter intensities  $\sigma_{wSpd}$ . The red solid curve is derived using a least-squares method based on a third-degree polynomial function as in [15].

## 2.2 Modified Curve-fitting-based Algorithm

In addition to rain recognition, a more comprehensive data control process is incorporated. The procedure includes the recognition of low-backscatter images. Then, a dual-curve-fitting technique is proposed here to improve the accuracy of wind retrieval from images under low sea states.

### 2.2.1 Low-backscatter Image Recognition

As a result of too-low wind speed or unknown system errors, some images may appear almost completely black with little or no wave signature. These images are referred to as low-backscatter images. A parameter, referred to as the low-clutter direction percentage (LCDP), is used for specifying low-backscatter images. If the ZPP of an azimuthal direction, which is empirical and also varies with systems, is higher than 40% for the Decca or 80% for the Furuno radar, the direction is considered to be a low-clutter (including blockage) direction. Then, if the LCDP, i.e., the number of low-clutter directions divided by the number of pulses, of an image is higher than 90%, the image is recognized as a low-backscatter image (see Fig. 2.1(c)) and is not used for wind retrieval.

### 2.2.2 Dual-curve-fitting

To retrieve wind direction from an individual image, the radar backscatter intensities from the non-obstructed antenna look directions are averaged over range to perform the curve-fitting. The data in the directions due to blockage were excluded. However, for some images, in many azimuthal directions a majority of the pixels may

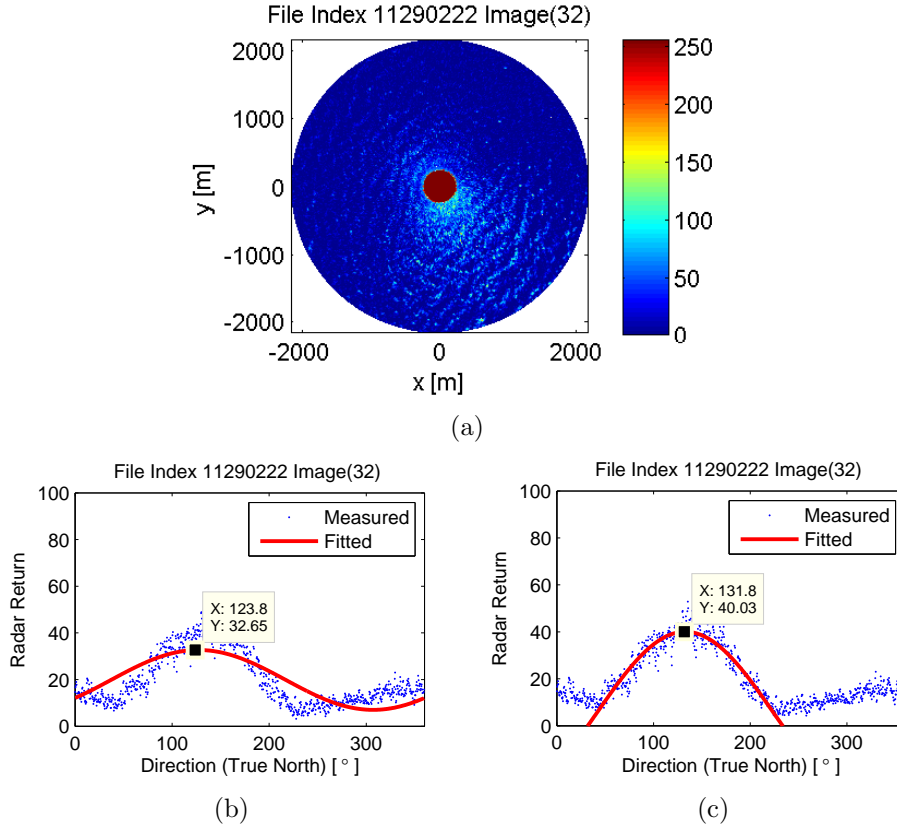


Figure 2.4: Example of the Decca radar data from Dataset 1 (collected at 02:22, Nov. 29, 2008): (a) backscatter image; (b) range-averaged backscatter intensity as a function of antenna look direction using single-curve-fitting; (c) range averaged backscatter intensity as a function of antenna look direction using dual-curve-fitting.

have a very low intensity (see Fig. 2.4(a)). These regions with low intensities are not due to the obstruction by ship structures but probably result from low sea states. These low-intensity data are retained in the curve-fitting process. Unfortunately, as shown in Fig. 2.4(b), in these low-intensity azimuthal directions, the single-curve-fitting result is not ideal. In this case, a dual-curve-fitting may be implemented. The technique involves repeating curve-fitting using the data at angles of  $60^\circ$  to the left and right of the first-guess upwind direction. Since the data in the directions around the direction with maximum backscatter (upwind) usually have higher signal-to-noise ratio (SNR) than the data in other directions, using this portion of the data for curve fitting leads to a more robust result. The direction range chosen for the second-

curve-fitting should be wide enough to include the upwind direction. However, if this range is too large, performance may be affected because data with low SNR may be included. If the range is chosen to be too large, the upwind peak may be missed and the fitting result may not be good due to a small number of data points. The  $\pm 60^\circ$  range is chosen since it yields satisfactory results. In the example shown in Fig. 2.4(c), the dual-curve-fitting results in an improvement of about  $8^\circ$ , as compared to that obtained using a single-curve-fitting. It should also be noted that, when the dual-curve-fitting is applied, the non-positive fitted values are excluded for evaluating the average radar backscatter intensity  $\sigma_{wSpd}$ .

## 2.3 Results

The data used for testing were provided by DRDC. The marine radars utilized in the experiment are standard ship-borne Decca (BridgeMaster II 340) and Furuno (7041 R) nautical radars which operate at 9.41 GHz. The Decca and Furuno radars cover  $360^\circ$  in azimuth with approximate beam width of  $2^\circ$  and  $1.9^\circ$ , respectively. The radar range extends to 2160 m (starting at 240 m in the near range) with a range resolution of 7.5 m. The radar was connected to a WaMoS II [5]. The system digitizes the radar backscatter intensities by azimuth-range bin and scales data into 8-bit unsigned integers ( $[0, 255]$ ). Sets of 32 radar images are combined into one file, and the file index reveals the start time of each file.

The information of the data used in this paper is listed in Table 2.1. The collection times are shown in standard local time. All radar images are oriented to true North. It should be noted that the first three datasets were collected during the same sea trial but Dataset 4 was collected from another experiment. The shipborne anemometer (Young Meteorological, Model 05106) and marine radar data were all collected on the Canadian Navy research ship CFAV Quest [65] approximately 150 miles from the

Table 2.1: Data Information

| Dataset No.                    | 1   | 2                               | 3                               | 4                               |
|--------------------------------|---|---------------------------------|---------------------------------|---------------------------------|
| Antenna                        | Decca   | Furuno                          | Decca                           | Furuno                          |
| Rotation Rate (RPM)            | 28  | 40                              | 28                              | 40                              |
| Collecting Time                | Nov.26, 23:45-<br>Nov.28, 04:04;<br>Nov.28, 11:16-<br>Nov.29, 12:06 | Dec.01, 12:09-<br>Dec.04, 12:02 | Nov.29, 01:12-<br>Nov.29, 05:31 | Oct.29, 17:46-<br>Oct.29, 18:46 |
| No. of Radar Images            | 49182   | 69088                           | 3872                            | 992                             |
| No. of Rain Cases              | 9924  | 992                             | 0                               | 0                               |
| No. of Low-back-scatter Images | 1832  | 8837                            | 224                             | 0                               |

coast of Halifax ( $42^\circ$  N,  $62^\circ$  W) in late October, late November and early December, 2008 [11]. Two anemometers were installed in the port and starboard side, respectively. Only the data measured by the starboard side anemometer is used because the wind results from these two anemometers are very similar. Since the heights of the anemometers are not available, the wind data could not be converted to the corresponding values at 10 meters above the water. The anemometer wind data were affected by the ship's motion. Thus, the reference wind speed and direction are calculated by removing the ship's motion, for which only the ship velocity over ground is considered here. Dataset 3 is a 4-hour subset of dataset 1 which includes the data under low sea states, and it is used to compare the performance of dual-curve-fitting and single-curve-fitting under low sea states. Dataset 4 is a 1-hour dataset collected in late October by a Furuno radar. This dataset is employed to test the modified ILS based algorithms with respect to island recognition and removal (See Chapter 3).

The single-curve-fitting and dual-curve-fitting based algorithms described above were applied to the quality-controlled Decca and Furuno radar data and the results were compared to the reference data measured by a ship-based anemometer (with the ship's motion removed). Since it must take a finite amount of time for the ocean

roughness to react to wind change, unlike the anemometer, the radar may not sense short time scale wind variations. As is commonly done, 10-minute averaging was applied to both the anemometer and radar wind results before computing the comparison statistics. The same data, excluding rain-contaminated and low-backscatter cases, were used to determine the wind speed calibration functions for both single- and dual-curve-fitting. Since the radars for Dataset 1 and 2 are different, wind speed models were developed for each of the two radars. The data over the periods of 11:16 Nov. 28 - 11:58 Nov. 29 in Dataset 1 and 12:08 Dec. 1 - 21:20 Dec. 2 in Dataset 2 were used for training for the Decca and Furuno radars, respectively. The wind speed standard deviations (STDs) of the Decca training and validation (non-training) data are 1.2 m/s and 1.7 m/s, respectively, while for the Furuno radar, they are 1.6 m/s and 2.0 m/s, respectively. Thus, the statistics do not differ significantly between the training and validation subsets. The statistics of the wind results for the first 3 datasets utilizing the single- and dual-curve fitting are shown in Table 2.2.

Fig. 2.5 shows the comparison of the radar-derived wind velocities using single- and dual-curve-fitting methods with the anemometer-measured results based on Dataset 3 collected during 01:12 to 05:31, Nov. 29, 2008. It can be seen that the radar results from both methods agree well with the anemometer data. Taking the anemometer results as the ground truth, the STDs of wind direction and speed using single-curve-

Table 2.2: Wind speed and direction error statistics: bias and STD

| Dataset No.        | Algorithm            | Wind Direction Error |         | Wind Speed Error |           |
|--------------------|----------------------|----------------------|---------|------------------|-----------|
|                    |                      | Bias [°]             | STD [°] | Bias [m/s]       | STD [m/s] |
| 1                  | Single Curve Fitting | 1.5                  | 15.3    | 0.4              | 1.4       |
|                    | Dual Curve Fitting   | 1.8                  | 14.9    | 0.4              | 1.4       |
| 2                  | Single Curve Fitting | 1.2                  | 17.0    | 0.3              | 2.0       |
|                    | Dual Curve Fitting   | 1.1                  | 16.6    | 0.2              | 1.9       |
| 3                  | Single Curve Fitting | 1.7                  | 8.3     | 0.8              | 0.9       |
|                    | Dual Curve Fitting   | 1.1                  | 6.6     | 0.7              | 0.8       |
| 3 (Low Sea States) | Single Curve Fitting | 9.1                  | 3.4     | 1.7              | 0.2       |
|                    | Dual Curve Fitting   | 3.4                  | 3.5     | 1.4              | 0.2       |

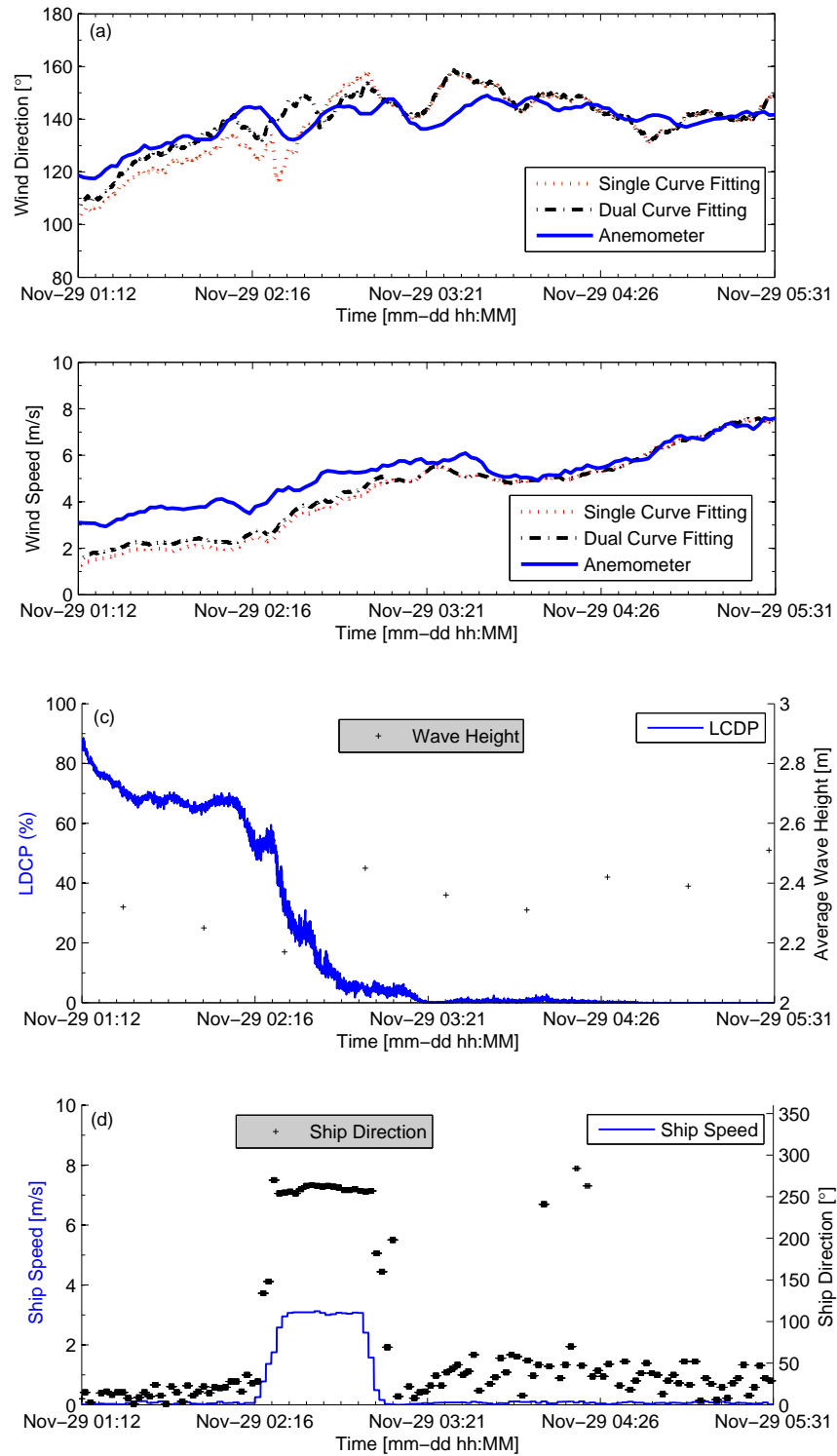


Figure 2.5: Comparison of wind results using Dataset 3 (Decca) from 01:12 to 05:31, Nov. 29, 2008: (a) wind direction; (b) wind speed; (c) significant wave height and percentage of directions with many low intensity pixels; (d) ship speed and ship direction.

fitting are found to be  $8.3^\circ$  and  $0.9$  m/s, respectively, and those for dual-curve-fitting are, respectively,  $6.6^\circ$  and  $0.8$  m/s (see Table 2.2). It is known that the sea surface roughness increases with wind speed. The buoy-measured significant wave heights are plotted in Fig. 2.5(c) for illustration. As shown in Fig. 2.5(a), improvement using dual-curve-fitting is seen during 01:12 to 02:22 when the sea states were low (significant wave height lower than 2.30 m). During this period, based on the low-clutter direction percentage analysis, the percentage of directions with many low intensity pixels is above 50% (see Fig. 2.5(c)). Within this 70-minute period, the STDs of wind direction and speed using single-curve-fitting are  $3.4^\circ$  and  $0.2$  m/s, respectively, and those for dual-curve-fitting are, respectively,  $3.5^\circ$  and  $0.2$  m/s. Although the STDs are almost the same, the mean errors of wind direction and speed have been improved by about  $5.7^\circ$  and  $0.3$  m/s, respectively, during low sea states. The performances of the single- and dual-curve-fitting techniques are almost the same when the wind speed is higher than  $4$  m/s, under which condition the clutter is strong in almost all azimuthal directions (see Figs. 2.5(b) and (c)). Further comparisons for wind results using different algorithms will be discussed in the following chapter (Section 3.3).

## 2.4 General Chapter Summary

In this chapter, the curve-fitting-based algorithms for wind retrieval from shipborne X-band nautical radar images were investigated. A more specific data quality control process was performed for each image, including the recognition of rain and low-backscatter images. Then, based on the single-curve-fitting method [15], a dual-curve-fitting approach was proposed to improve the accuracy of wind direction. With the dual-curve-fitting algorithm, the wind direction and speed mean difference between the radar and anemometer results can be reduced by about  $5.7^\circ$  and  $0.3$  m/s, respectively, under low sea states. However, the results obtained from single- and dual-curve-fitting are almost the same at higher sea states. In the next chapter, an

intensity-level-selection based algorithm is implemented for wind field recovery.

# Chapter 3

## ILS-based Wind Algorithms

In this chapter, the intensity-level-selection (ILS) based algorithm for sea surface wind retrieval from shipborne X-band nautical radar images is first presented. Next, the modified ILS-based method which consists of data quality control and range distances vector curve-fitting is proposed. Finally, the wind results obtained from the same radar data described in Chapter 2 using these two ILS-based algorithms are compared with the shipborne anemometer data, and the performance of the two improved methods (i.e., dual-curve-fitting and the modified ILS-based algorithms) is evaluated.

## 3.1 Original ILS-based Algorithm

This section introduces the original ILS-based method, which includes the temporal integration and spatial smoothing of a set of consecutive radar images, intensity-level-selection, and wind direction and speed estimation [17]. The block diagram of the original ILS-based wind algorithm is shown in Fig. 3.1.

### 3.1.1 Temporal Integration and Smoothing

For the data presented in this research, since each radar image has 288 range bins (including 32 bins associated with the dead range) but a different number of pulses, the radar images cannot be directly summed. Interpolation to a standardized grid is implemented to generate radar images with a uniform size of 1024 (pulses)  $\times$  288 (ranges). The temporal integration is performed on the entire sequence of files (many hours of data) by utilizing a moving average of every 32 radar images with a shift of four images. As in [17], each time average result is further smoothed over five range cells (two leading and two lagging with the result being assigned to the central cell) and an azimuthal extent of  $5^\circ$ . As addressed below, each integrated image is assigned a certain intensity level and associated range distances vector, from which the wind information can be extracted.

### 3.1.2 Intensity-level-selection

The general technique is given in [17] and the particulars of its present application follow. By analyzing the histograms of the integrated radar images  $I_i$ , the predefined levels set for both radars in our study were chosen as  $L_1 = 5$ ,  $L_2 = 10$ , ...,  $L_{25} = 125$ , on a scale of 0 to 255. For each integrated image, an optimal intensity level is selected adaptively (see Fig. 3.1). The algorithm for selecting the intensity level  $L_i$  operates as follows:

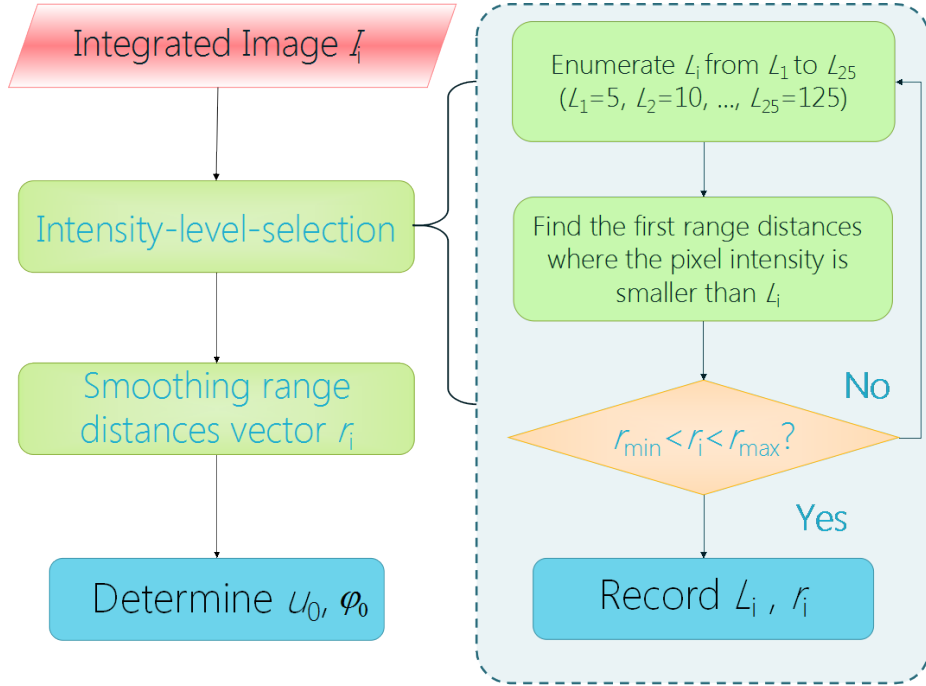


Figure 3.1: Block diagram of the original ILS-based wind algorithm.

1. Startup. In each of the first 8 integrated images, for each predefined intensity level  $L_i (i = 1, 2, \dots, 25)$ , the first range distance where the backscatter intensity is smaller than  $L_i$  is sought in each azimuthal direction. All the smoothed range distances associated with each  $L_i$  are then stored as elements of the smoothed range distances vector  $r_i^s$ . From these vectors, the one with the lowest  $L_i$ , for which all elements are greater than the inner distance boundary (the near-range distance boundary plus a guard range (i.e., dead range of the radar display,  $7.5 \times 32 \text{ m} + 75 \text{ m} = 315 \text{ m}$ )), is selected.
2. After the first 8 integrated images, only the last selected level  $L_i$  and its two adjacent intensity levels  $L_{i+1}$  and  $L_{i-1}$  need to be used to obtain three corresponding range distances vectors. Among these three vectors, the one satisfying the inner distance boundary and having the lowest intensity level is used for wind direction retrieval and is referred to as the smoothed retrieval range distances vector  $r_i^s$ .

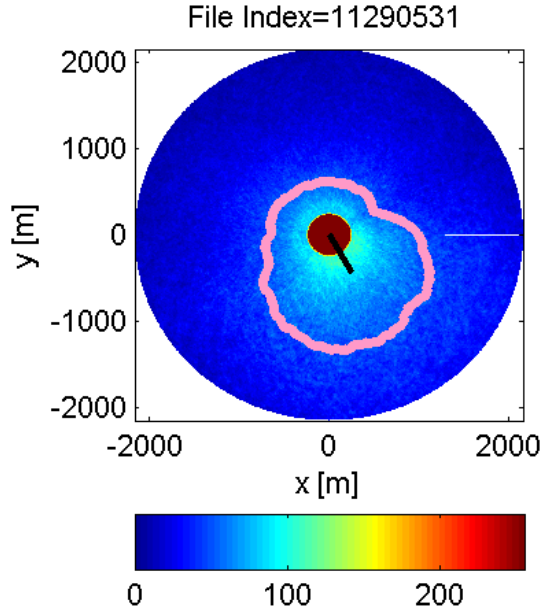


Figure 3.2: An integrated radar image without blockage.

3. Adaptive adjustment. When an anemometer-measured wind speed decrease is observed, a slight decrease of the selected level is applied, and vice versa.

In the case of Fig. 3.2, the selected intensity level from all the predefined levels is  $L_i = 60$ . Its smoothed range distances vector for  $L_i = 60$  is plotted as a pink ring.

### 3.1.3 Wind Direction

The algorithm for wind direction retrieval is based on the radar backscatter intensity dependence on antenna look direction. The wind direction  $\phi_0$  is determined to be along the azimuth in which the maximum of the smoothed range distances vector is located in the integrated image. In Fig. 3.2, the wind direction determined from the smoothed range distances vector maximum is  $139^\circ$  (with respect to true North), while the reference wind direction (see the black bar) is  $150^\circ$ .

### 3.1.4 Wind Speed

It is assumed that wind speed  $u_0$  is related to the maximum of the retrieval range distances vector corresponding to the selected intensity level  $L_i$  as

$$u_0 = \alpha_i \times \max\{r_i^s\} \quad (3.1)$$

where  $\max\{r_i^s\}$  is the maximum of the smoothed retrieval range distances vector and  $\alpha_i$  represents the conversion rate corresponding to the selected intensity level  $L_i$ . However, the relationship between  $\alpha_i$  and  $L_i$  is nonlinear and can be fitted by the third-order polynomial function [17]

$$\alpha_i = \beta_3 L_i^3 + \beta_2 L_i^2 + \beta_1 L_i + \beta_0 \quad (3.2)$$

in which the parameters  $\beta_j (j = 0, 1, 2, 3)$  can be determined by least-squares fitting. The fitting is implemented based on the obtained  $L_i$  and  $\alpha_i$  that is calculated from Eq. (3.1) using *in-situ* wind speed and  $\max\{r_i^s\}$ . Fig. 3.3 shows the conversion rate function obtained from Dataset 2. Red dots and blue stars, respectively, represent the fitted and the calculated  $\alpha_i$ . After the polynomial function is obtained, wind speed is calculated from the maximum range distance associated with  $L_i$  and the selected  $\alpha_i$ .

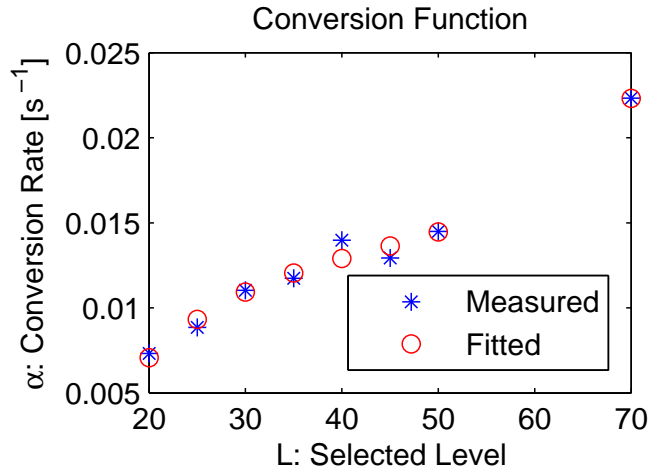


Figure 3.3: Conversion function model obtained using Dataset 2 (Furuno).

## 3.2 Modified ILS-based Method

In this section, the modifications have been made to improve the robustness of the ILS algorithm. These include an additional constraint setting for intensity level selection, the recognition of blockages and islands for data quality control, and a curve-fitting technique applied to the range distances vector.

### 3.2.1 Blockage Recognition

For the data considered in this section (Datasets 2 and 4), shadowing of the radar field of view exists in many images (see the example in Fig. 3.4(a)). The broken part of the selected range vector (marked as an open pink ring) indicates the blocked area. It should suffice to determine the blockage once for each radar station if the blockage is due to a stable ship structure. However, the real-time monitoring of blockage will allow the algorithm to be applied to a broader class of conditions which accounts for the fact that there may be blockage induced by severe weather or when operators deliberately or otherwise block data from a particular sector, but in no particular pattern. In such cases, each integrated image should be subjected to real-time blockage recognition. If the percentage of zero pixels is higher than 20% in a particular direction, this direction is considered to be blocked and the data located in this part of the integrated image are discarded. Otherwise, the ILS algorithm may fail to produce a qualified predefined level.

### 3.2.2 Curve-fitting

After discarding the obstructed data, problems may still exist, as shown in Fig. 3.4(a). If the wind direction is aligned with the blocked angles, the above mentioned algorithm will not produce the correct direction. Inspired by the work in [15], a harmonic

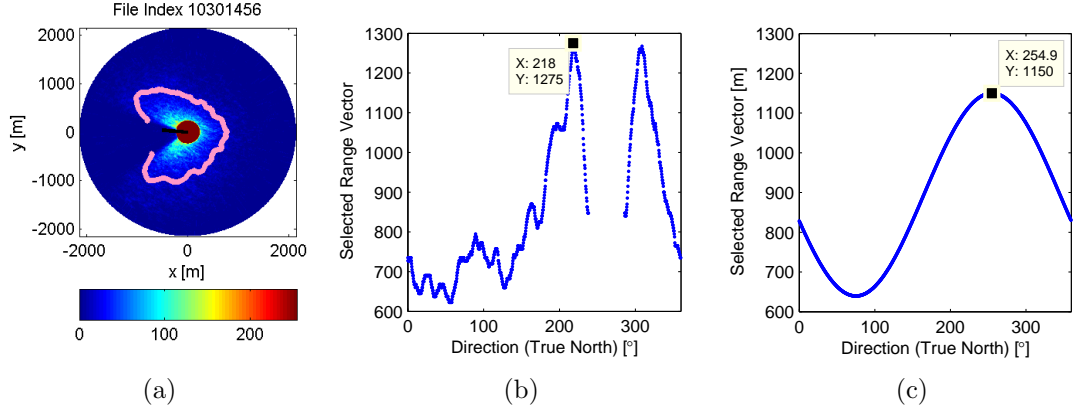


Figure 3.4: A blockage case: (a) an integrated image with blockage; (b) the selected range distances vector referred to (a) before curve-fitting; (c) the selected range distances vector referred to (a) after curve-fitting.

function, similar to Eq. (2.1),

$$r_i^s(\phi) = b_0 + b_1 \cos^2(0.5(\phi - b_2)) \quad (3.3)$$

was introduced to fit the selected range vector  $r_i^s$  (see Figs. 3.4(a)-(c)). In Eq. (3.3),  $b_0$ ,  $b_1$ ,  $b_2$  are coefficients to be determined by curve-fitting. Usually, the locus of the tip of the range vector forms a cardioid. This property can be utilized to avoid multiple maxima situations and improve the accuracy of wind direction determination. In Fig. 3.4(b), the range distances vector maximum is  $218.0^\circ$  and is corrected by curve-fitting to  $254.9^\circ$  (with respect to true North) as shown in Fig. 3.4(c), while the corresponding anemometer measured wind direction is  $275.2^\circ$  (see Fig. 3.4(a)). Therefore, the gap in the original range vector plot can be filled.

### 3.2.3 Island Recognition

In Fig. 3.5(a), a large object (green area in the top left corner) appears in the integrated image. By observing the ship's track, indicated by the blue dots in Fig. 3.5(c), it was found that at the time of Fig. 3.5(a) (18:00 Oct. 29, 2008), the ship's position to which the red arrow points in Fig. 3.5(c) is very close to the coastline (black line

pointed by a black arrow). Thus, the object is probably a small island. In the wind direction algorithm, the first range index where the intensity is smaller than the pre-selected intensity level  $L_i$  is chosen. It can be inferred that if the island is located in the far range, the island's influence can be automatically neglected. However, when the island is close to the ship, estimation of the maximum range for  $L_i$  and the wind direction may be incorrect (see Fig. 3.5(a)). In this case, by utilizing the attenuation property of the radar backscatter intensity along range, if an intensity bump is detected in an azimuthal direction, it is assumed that the island is located in that direction and the corresponding radar data will be excluded from curve-fitting (see Fig. 3.5(b)). The built-in function, `findpeaks`, in Matlab is used here to detect peaks or extrema of the intensity sequence for each azimuthal direction. Geographic data may be used to replace the island recognition scheme if such data are available.

### 3.3 Results

The original ILS and modified ILS-based algorithms were applied to the same radar data as described in Table 2.1, and the results were compared to the anemome-

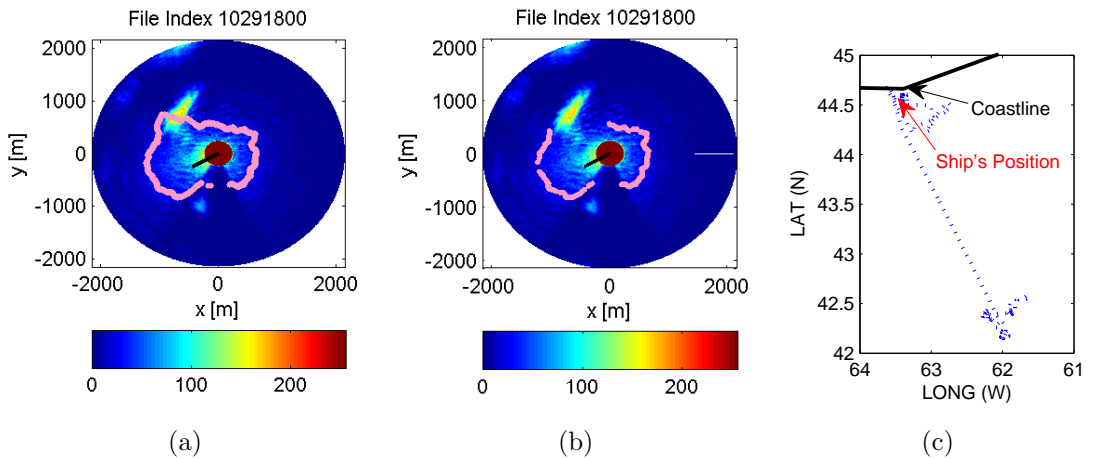


Figure 3.5: Illustration of island recognition using Dataset 4 (Furuno): (a) range distances vector (pink line) without island recognition; (b) range distances vector with island recognition; (c) map with ship's track.

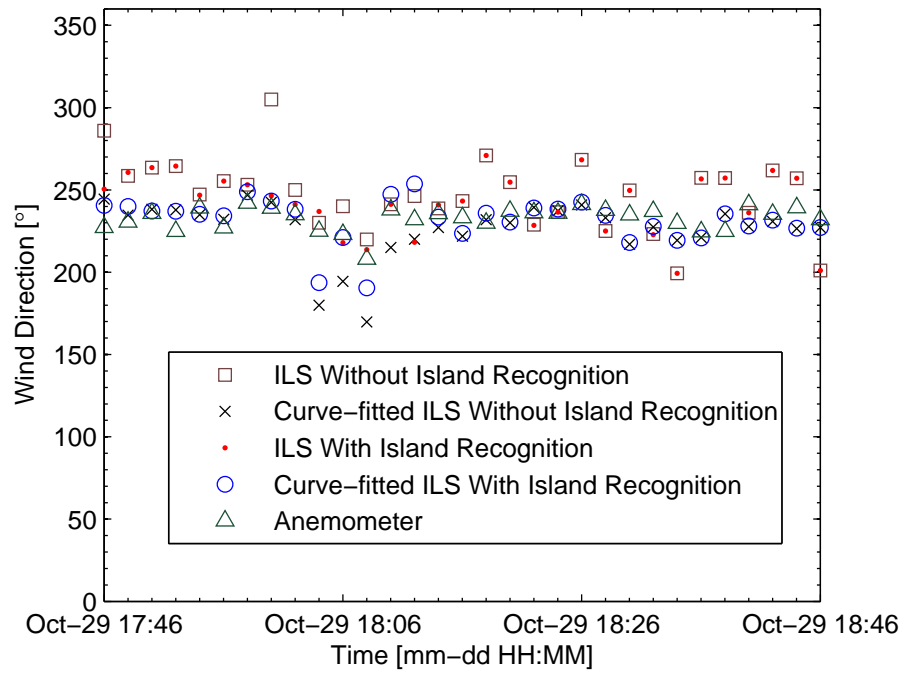
ter data. Additionally, the performance of the modified curve-fitting and ILS-based algorithms are also evaluated here. The statistics of the wind results for each entire dataset utilizing the original and modified ILS based algorithms are shown in Table 3.1.

### 3.3.1 Original ILS vs. Modified ILS

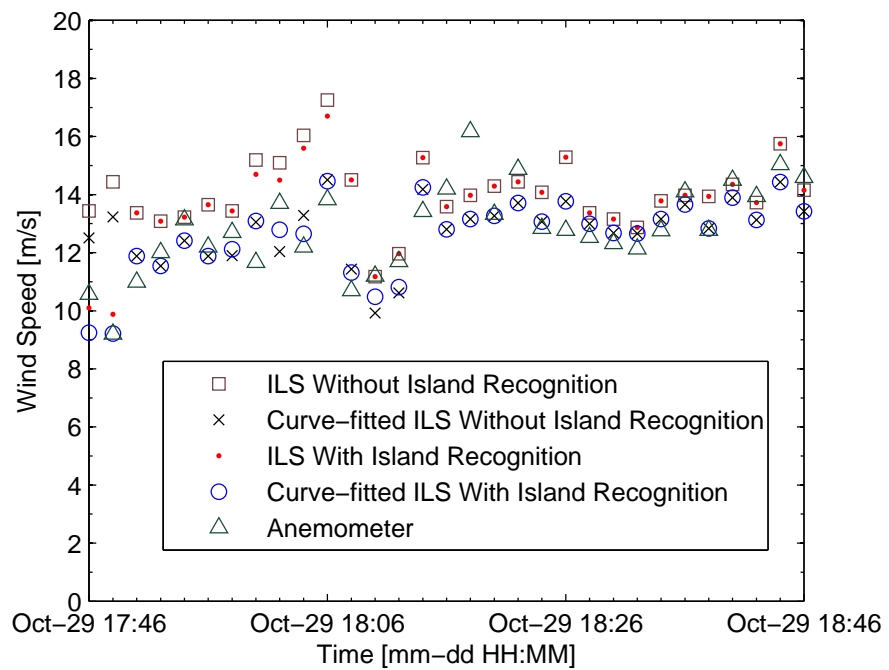
Fig. 3.6 shows the results with and without island recognition from Dataset 4, during 17:46 to 18:46, Oct. 29, 2008, which involves the period when ship approached and then left the island from 17:56 to 18:16. The island was located in the near range from 18:00 to 18:10 when the results using island recognition show some improvement (the STDs of retrieved wind direction and speed are reduced by about  $7^\circ$  and 0.3 m/s, respectively, from those measured by the anemometer, as shown in Table 3.1). It may be observed that from 17:46 to 17:58 and 18:12 to 18:46, the wind results with island recognition are exactly the same as those without island recognition. This is because the island was located far from the ship during these periods, and the ILS algorithm itself can withstand the island interference automatically. Also, it can be seen that the results using the curve-fitted ILS-based method are more stable than those obtained using the original method (see Fig. 3.6).

Table 3.1: Wind speed and direction error statistics: bias and STD

| Dataset No. | Algorithm                  | Wind Direction Error |                  | Wind Speed Error |           |
|-------------|----------------------------|----------------------|------------------|------------------|-----------|
|             |                            | Bias [ $^\circ$ ]    | STD [ $^\circ$ ] | Bias [m/s]       | STD [m/s] |
| 1           | ILS                        | 3.0                  | 20.8             | 1.2              | 1.5       |
|             | Modified ILS               | 1.7                  | 15.9             | 0.6              | 1.4       |
| 2           | ILS                        | 3.8                  | 21.2             | 1.1              | 1.5       |
|             | Modified ILS               | 0.8                  | 16.3             | 0.6              | 1.3       |
| 3           | ILS                        | 4.4                  | 10.3             | 0.3              | 0.8       |
|             | Modified ILS               | 1.9                  | 9.3              | 0.3              | 0.5       |
| 4           | Without Island Recognition | 14.1                 | 18.8             | 0.2              | 1.3       |
|             | With Island Recognition    | 1.3                  | 11.8             | 0.1              | 1.0       |



(a)



(b)

Figure 3.6: Comparison results obtained from Dataset 4 (Furuno) with appearance of island: (a) wind direction; (b) wind speed.

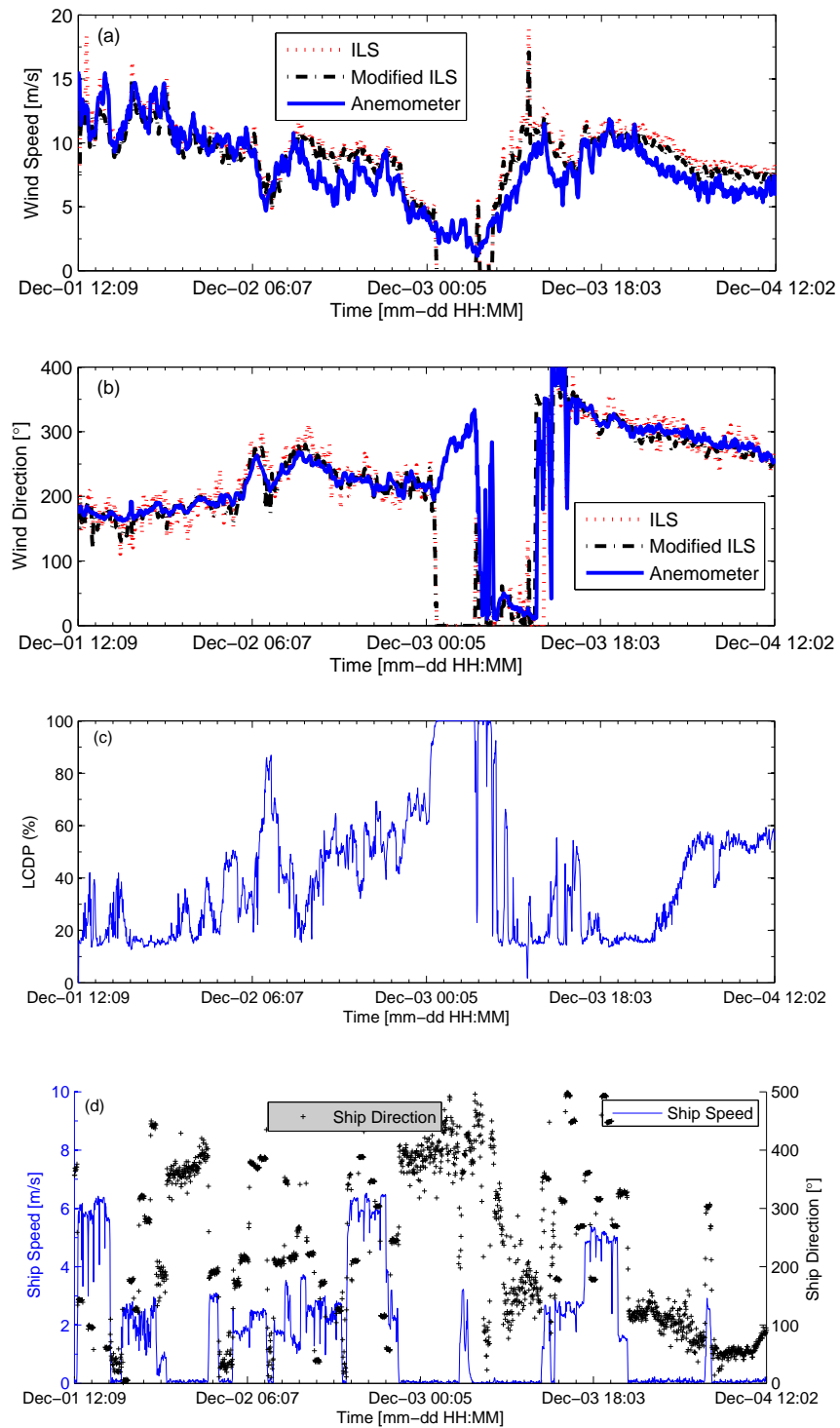


Figure 3.7: Comparison of wind results using ILS and modified ILS-based algorithms for Dataset 2: (a) wind direction; (b) wind speed; (c) low-clutter direction percentage; (d) ship speed and ship direction.

Next, the modified ILS method above was applied to a longer dataset of quality-controlled Furuno radar data and the results were compared with the reference data measured by a shipborne anemometer (with the ship’s motion removed). Fig. 3.7 shows the comparison of the radar-retrieved wind velocities obtained from the original and modified ILS-based methods with the anemometer-measured results based on Dataset 2 collected during the period from 12:09, Dec. 1 to 12:02, Dec. 4, in 2008. It may be observed that the radar results from both methods agree well with the anemometer data. However, the results using the modified method are clearly more stable with respect to the wind direction results even when more than half of the image data are discarded due to blockage and low wind speed from 06:30 to 07:30, Dec. 2 (see Figs. 3.7(a)-(c)). From 00:30 to 06:00, Dec. 3, the low-clutter direction percentage is higher than 90%, so those images are considered as low-backscatter cases and are discarded. Moreover, the influence of frequent ship motion on the anemometer-measured results is observed around 05:00 and 15:00, Dec. 3 in Fig. 3.7(a). The anemometer winds appear more spiky than the radar results. From Fig. 3.7(d), it can be seen that the ship motion changed significantly and frequently. For all the Furuno data collected in December, it is shown that the modified ILS-based method reduces the mean differences and STDs between the radar and anemometer results for wind direction and speed by about  $3^\circ$  and  $4.9^\circ$  and  $0.5$  m/s and  $0.2$  m/s, respectively (see Table 3.1).

### 3.3.2 Dual-curve-fitting vs. Modified ILS

By comparing the wind parameter results obtained from Dataset 1 using the modified ILS-based and dual-curve-fitting algorithms with the anemometer data, it may be observed from Fig. 3.8 that both algorithms can provide satisfactory results in most cases. When the zero pixel percentage is lower than 10% (see Fig. 3.8(d)) in this dataset, the data are classified as rain cases. Rain was recognized during 02:10

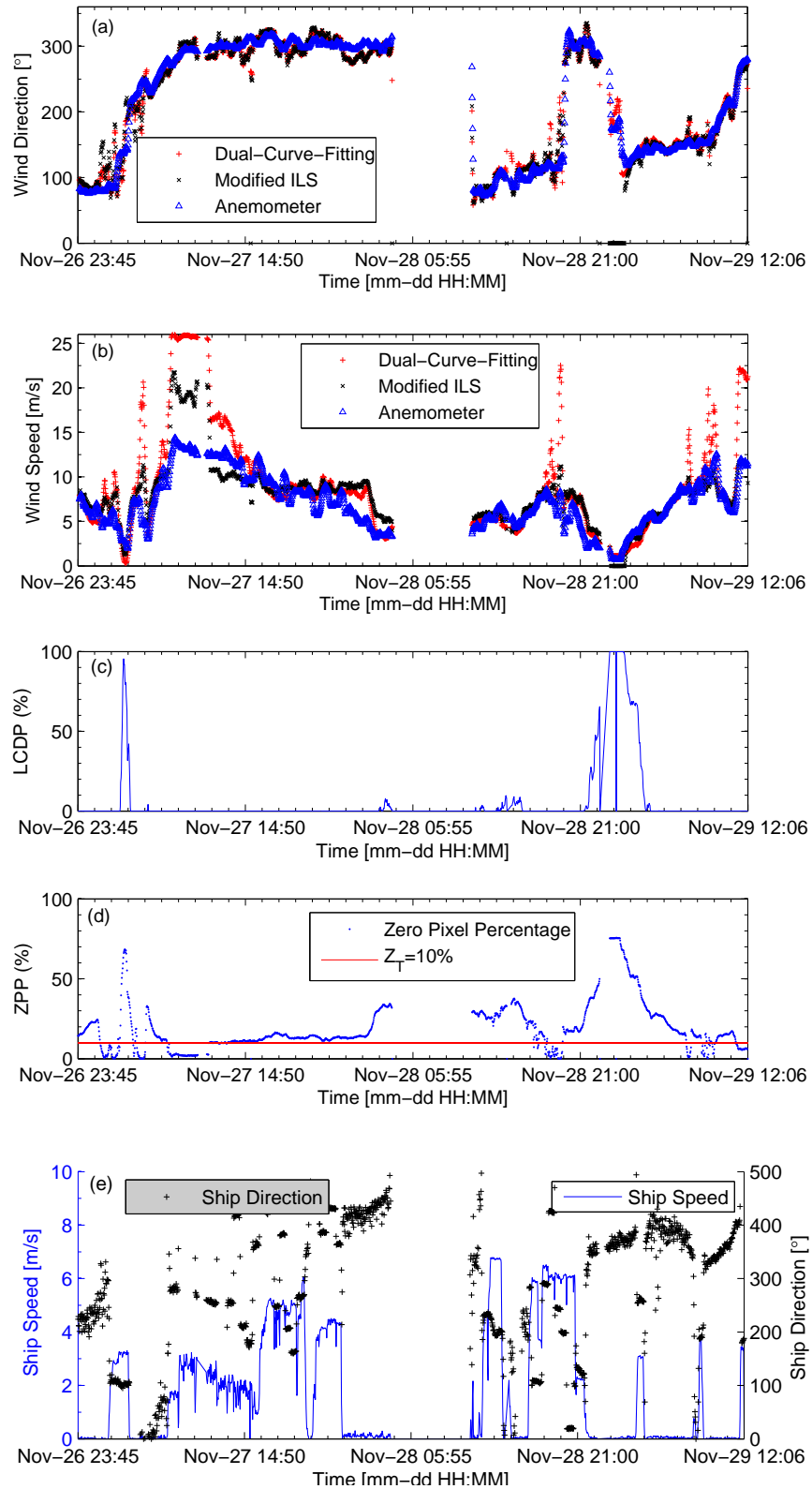


Figure 3.8: Comparison results using dual-curve-fitting and modified ILS-based algorithms for Dataset 1: (a) wind speed; (b) wind direction; (c) low-clutter direction percentage; (d) zero pixel percentage; (e) ship information.

to 05:40 and 08:10 to 13:30 on Nov. 27, 18:00 to 19:30 on Nov. 28, and 06:40 to 09:10 on Nov. 29, when the STDs and mean errors of wind speed and direction between the reference data and the retrieved wind results using both methods are larger than under the rain-free condition. It was also found that when rain interference exists, the modified ILS method seems more robust than the dual-curve-fitting method for the data considered here. For example, during 11:40 to 12:06, Nov. 29, the wind speed by dual-curve-fitting is significantly overestimated due to rain, while the result from the modified ILS-based method is satisfactory. Similar conclusions can be made for the period of 08:00 to 10:00, Nov. 27. This may be because, based on our calibration model (see Fig. 2.3) for the curve-fitting method, a small increase in intensity will cause a relative large increase in wind speed when the speeds are within 13-20 m/s. However, the ILS-based model seems less sensitive to intensity change over that speed range. A better model with more training data at high wind speeds may improve the wind results obtained from the curve-fitting-based method. On the other hand, dual-curve-fitting shows superiority over the modified ILS method for wind direction when the low-clutter direction percentage is high due to low sea states (see the peak during 22:16, Nov. 28 to 01:13, Nov. 29 in Fig. 3.8(c)). The average execution times for processing a set of 32 radar images using dual-curve-fitting and the modified ILS algorithm are 6.001 s and 21.919 s, respectively, running in Matlab on an i5-3450 CPU of 3.10 GHz. On the other hand, the least time for collecting a set of 32 radar images is 48 s (for Dataset 2 or 4). Thus, it can be concluded that the modified approaches may be executed in near real time. The ILS-based algorithms take more time due to the dual-scan-conversion which, for our datasets, is implemented to standardize the image size before temporal integration. This procedure is not required in the curve-fitting based algorithms.

### 3.4 General Chapter Summary

In this chapter, the original and modified ILS-based algorithms for wind parameters extraction from shipborne X-band nautical radar images were investigated using radar and anemometer data collected on the Canadian East Coast. It is shown that the original ILS-based algorithm performs satisfactorily, and the modified ILS method is more robust than the original ILS-based method (reference algorithm), since the former can work well even when blockages or islands exist in the radar field of view. Although wind speed results extracted from the modified ILS method are not improved distinctly, maybe due to the quality of training, the modified ILS-based method reduces the mean differences and STD of wind direction between the radar and the anemometer results significantly by about  $3^\circ$  and  $4.9^\circ$  in Dataset 2. Moreover, it was found that the radar measurements from dual-curve-fitting and the modified ILS agree with each other for most of the data used here, and the mean difference and STD between the anemometer data and the radar results observed using the two improved algorithms for wind direction and speed are close.

One common limitation for the two improved algorithms is that the retrieved wind results from rain-contaminated data are worse than those under the rain-free condition. Thus, images in the presence of rain were discarded before wind speed and direction were extracted here. Further efforts were undertaken to design a method that may be used to recover wind parameters by exploiting the differences between images collected with and without rain. In the next chapter, an algorithm incorporating texture analysis is proposed for wind parameter recovery from rain-contaminated images.

## Chapter 4

# Wind Parameter Extraction from Rain-contaminated Radar Data

In the previous chapter, it has been observed that the results in the X-band radar-retrieved wind speeds are overestimated during rain. In this chapter, the effects of rain on X-band nautical radar images are investigated from both analytical and heuristic perspectives first. Next, a texture-analysis-based rain mitigation technique is proposed and incorporated into both the modified curve-fitting-based and ILS-based wind algorithms discussed previously.

## 4.1 The Effects of Rain

The effects of rain on X-band radar image intensity and the corresponding image spectrum are analyzed from an analytical perspective. Moreover, the effects of rain on wind parameter extraction using X-band radar images are summarized. The data analyzed here were extracted from Dataset 1 (see Table 2.1), since it contains more rain cases than the other datasets.

### 4.1.1 On Radar Intensity Images

Utilizing the integration and smoothing techniques in [17] to temporally integrate 32 consecutive radar images intensifies wind signatures. Fig. 4.1 shows the examples of individual radar images and the integrated images. Fig. 4.1(a) is a single radar

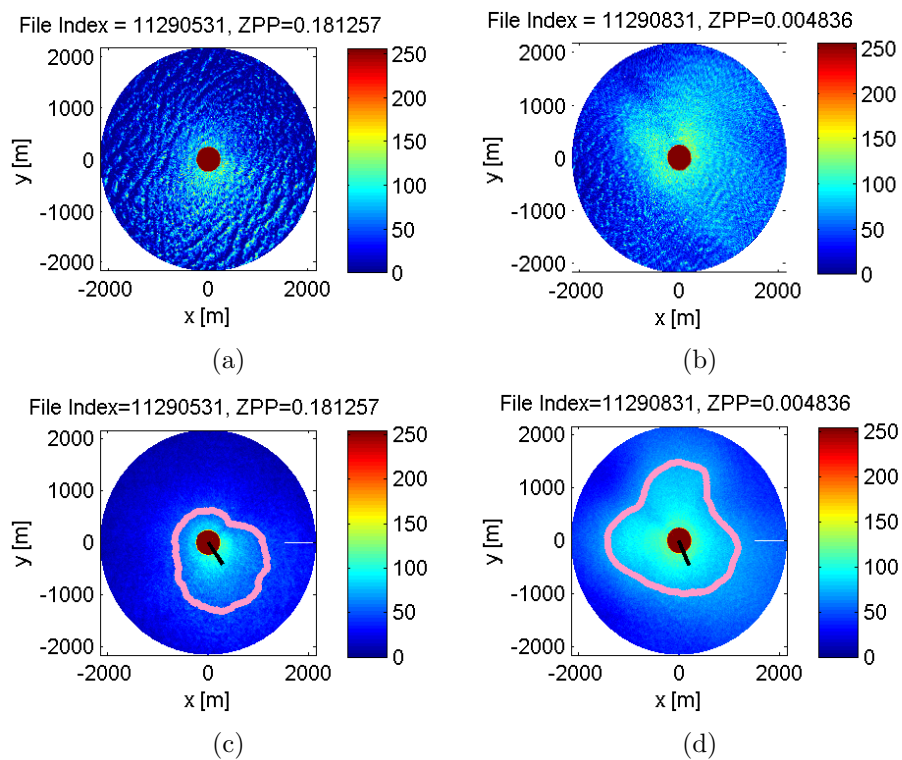


Figure 4.1: Examples of marine radar images: (a) single image without rain; (b) single image with rain; (c) integrated image without rain; (d) integrated image with rain.

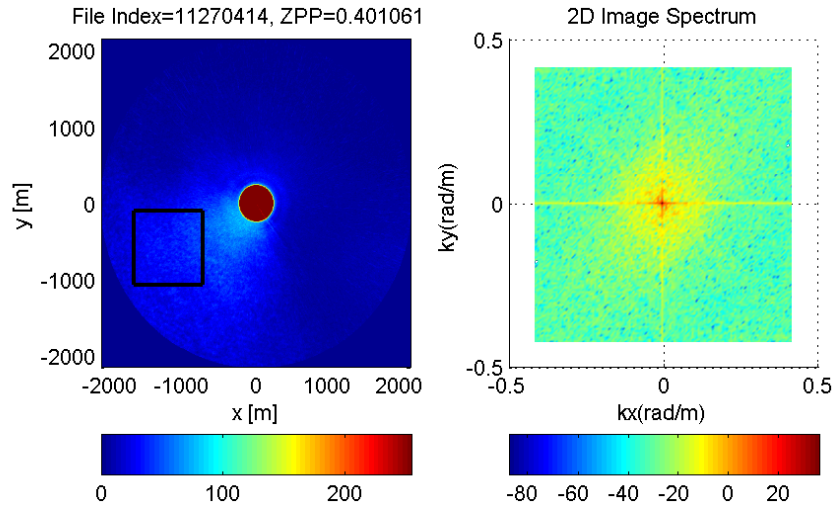
image collected at 05:31, Nov. 29, when it was not raining. Compared to Fig. 4.1(b), which is a single image collected at 08:31, Nov. 29, when rain was present, it can be clearly seen that the radar backscatter intensity is enhanced by rain. The rain contaminated image was also scaled to 0–255, but it looks more uniformly bright, which was similarly pointed out in [15]. Figs. 4.1(c) and (d) are temporally integrated images based on the corresponding single images including Figs. 4.1(a) and (b), respectively. It seems that wave signatures have been eliminated, while wind and rain signatures are intensified by integration.

### 4.1.2 On Radar Image Spectra

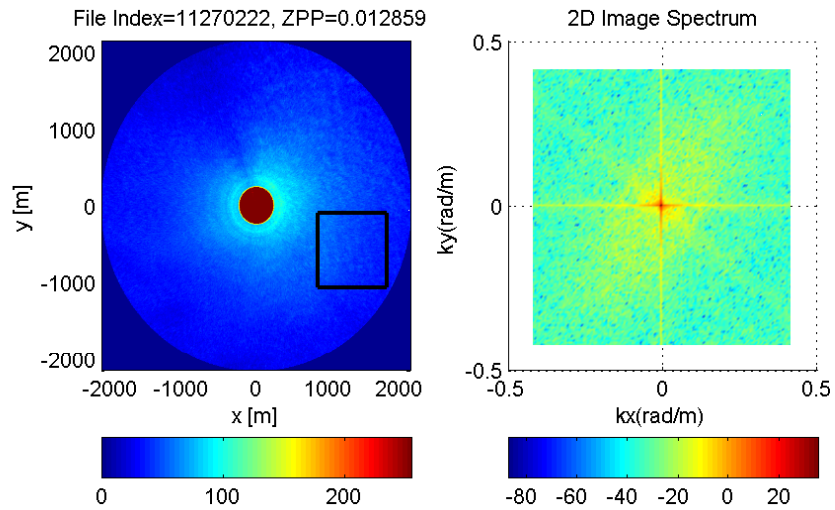
In [66], it was reported that two maxima, which are caused by radar backscattering from rain-generated ring waves propagating towards and away from the radar, are seen in the Doppler spectrum of an X-band coherent radar. A test is also implemented here to observe the rain signatures in the spatial frequency domain. After temporally integrating 32 consecutive Cartesian images, a  $128 \times 128$  rectangular window is selected to perform a 2-D FFT and generate an image spectrum (see the right most columns of Figs. 4.2(a) and (b)). It was found that energy falls in the area close to the zero-wavenumber point in the presence of rain. Again, this phenomenon may be explained by the elimination of wave signatures due to the contamination of rain. When the rain is absent, the energy spread is circular.

### 4.1.3 On Wind Parameters Extraction

Figs. 4.3(a) and (b) show wind parameter results incorporating the original and modified ILS-based methods. When the ZPP is lower than 10% (see the red line in Fig. 4.3(c)), the data are classified as rain cases. Rain was recognized during 02:10 to 05:40 and 08:10 to 11:30 on Nov. 27, 18:00 to 19:30 on Nov. 28, and 06:40 to 09:10 on Nov. 29 in 2008. Among these four periods with rain, it is observed from



(a)

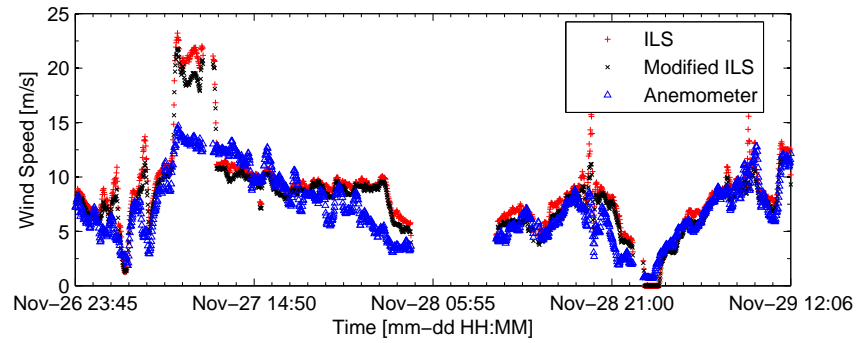


(b)

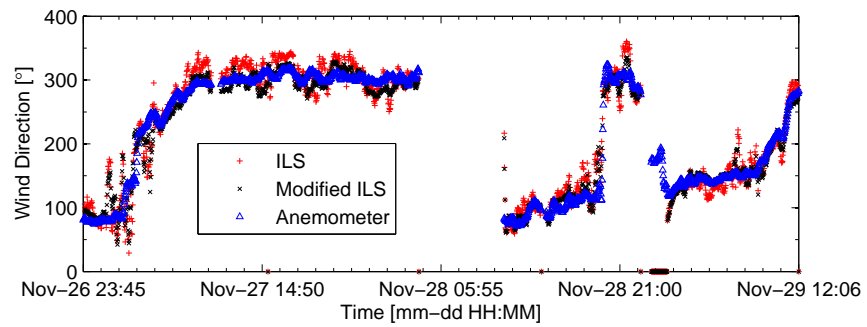
Figure 4.2: 2-D image spectrum: (a) in the absence of rain; (b) in the presence of rain.

Fig. 4.3(a) that the radar-retrieved wind speed was significantly overestimated during 08:10 to 11:30 on Nov. 27. For the data analyzed here, the STD of wind speed between radar retrieved results and the anemometer data is increased by about 1.6 m/s in the presence of rain from that in the absence of rain.

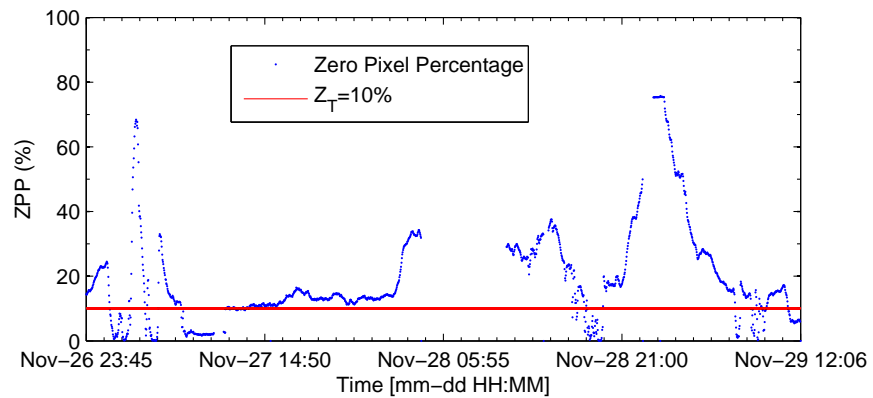
With respect to wind direction, it was deduced in [56] that rain may diminish the azimuthal variations. In [17], wind direction obtained from the ILS based method is assumed to be along the azimuth in which the maximum of the range distances



(a)



(b)



(c)

Figure 4.3: Wind field extraction comparison results using ILS based algorithms with and without rain: (a) wind speed; (b) wind direction; (c) zero pixel percentage.

vector is located. It was found that rain may negatively affect the recognition of the range vector maximum (see Fig. 4.1(d)). Usually, the locus of the tip of the range vector forms a cardioid which can be fitted to a harmonic function. This property can be utilized to avoid multiple maxima situations and improve the accuracy of wind direction determination as shown in [67], [68]. Nevertheless, even for the modified ILS-based method which employs curve fitting, the STD of wind direction in the presence of rain is increased by about  $10.7^\circ$ , taking the anemometer data as ground truth.

## 4.2 Detailed Methodology for Wind Algorithms Incorporating Rain Mitigation

In this section, the texture maps of X-band nautical radar images in the presence and absence of rain are analyzed. The wind algorithm incorporating the texture-analysis-based rain mitigation is then described.

### 4.2.1 Texture Analysis

From Section 4.1.1, it was illustrated that the rain-contaminated image pixels are more uniformly bright than the wave echoes, which implies that the characteristics of being “more uniformly bright” in the radar images may be used to identify the portions more affected by rain based on intensity spatial variability analysis. Referring to [62], the spatial variability is expressed as a root-mean-square (RMS) difference or texture,  $T$ , given as

$$T(I_{p,q}) = \sqrt{\frac{\sum_{i=-1}^{i=1} \sum_{j=-1}^{j=1} (I_{p,q} - I_{p+i,q+j})^2}{9}} \quad (4.1)$$

where  $I_{p,q}$  represents the radar backscatter intensity of the pixel  $(p, q)$ , in range  $(p)$  and in azimuth  $(q)$ . The texture of the original radar backscatter intensity  $T(I_{p,q})$  is computed in a box consisting of three pixels in azimuth and three in range centred on the gate. The corresponding texture maps of Figs. 4.4(a) and (b) are calculated as Figs. 4.4(c) and (d).

To ensure consistency with the original radar images, the texture intensities are scaled from 0 to 255 as well. It can be observed that, for the rain-free radar images, most of the wave signatures are retained in the texture map (see Fig. 4.4(c)). For the radar images contaminated by rain, radar signatures of waves are still visible on the portion between  $191^\circ$  and  $315^\circ$  (see the open pink arc in Figs. 4.4(b) and (d)), indicating that this portion may be less affected by rain. Actually, it is also revealed

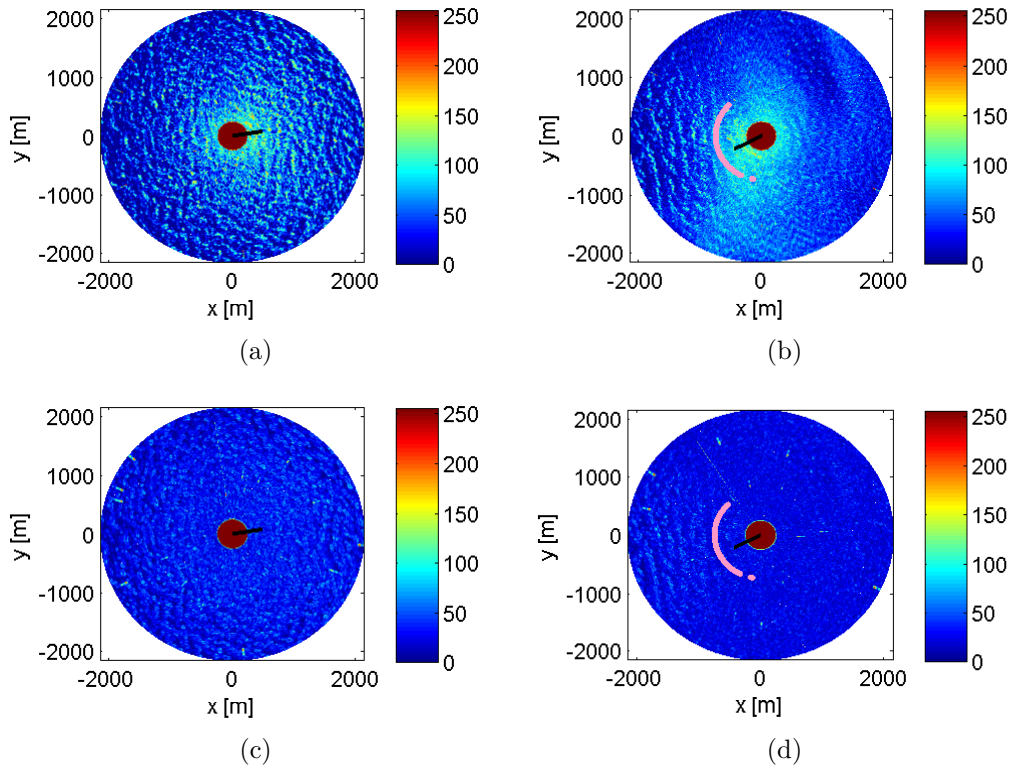


Figure 4.4: Examples of marine radar images and the their texture maps: (a) rain-free radar backscatter intensity image; (b) rain-contaminated radar backscatter intensity image; (c) rain-free texture map of (a); (d) rain-contaminated texture map (b).

from Figs. 4.4(b) and (d) that the image portion around the upwind direction is relatively less affected by rain than that around the downwind direction. This is because the upwind clutter is usually stronger than that from downwind [59]. Also, from the texture map in Fig. 4.4(d), it may be observed that the blurred or uniformly bright area in the original image of Fig. 4.4(b) has been removed (i.e. this portion becomes dark). This means that the rain-contaminated portion can be recognized from the texture map. This property will be utilized in the following sections to improve the accuracy of wind parameters estimation.

## 4.2.2 Data Filtering

Due to the strong impact of rain on the number of pixels with zero intensity, the ZPP was identified as a quality control parameter in determining the presence of rain [15]. In [15], when ZPPs are less than  $Z_T$  (10% for Dataset 1), these radar images were considered as contaminated by rain and discarded from the wind retrieval process. However, it was indicated in Section 4.2.1 that the less-rain-affected portions of the radar images may still be useful for sea surface parameter extraction (see Fig. 4.4(d)). A simple scheme is proposed here to recognize these portions of the rain-contaminated images. To mitigate the effects of rain on wind information extraction, those more-rain-affected portions in the identified rain-contaminated radar images will be removed from the wind retrieval process. Hence, this technique is referred to as Rain Mitigation.

Fig. 4.5 shows the block diagram of rain mitigation. For each azimuthal direction, in the original image, the number of pixels with intensity higher than a threshold  $I_T$  is recorded as  $N_\phi$ . If  $N_\phi$  is less than a specified value  $N_T$ , the data in such a direction will be identified as rain-contaminated. Figs. 4.6(a) and (b) show the number of data points  $N_\phi$  of the original images without and with rain, respectively. The thresholds  $I_T$  are empirically set to be 80 and 40 initially for the original image and texture

map, respectively, in this work. The rain threshold  $N_T$  is then adjusted adaptively according to the range of  $N_\phi$  since the threshold may differ under different wind speeds. Details of the threshold setting for  $N_T$  can be found in Fig. 4.5. For the data considered in Fig. 4.6, the threshold  $N_T$  is found to be 23. Figs. 4.6(c) and (d) depict the  $N_\phi$  of the texture maps of Figs. 4.6(a) and (b), respectively. It can be observed that  $N_\phi$  is greater than  $N_T$  in almost all directions in Fig. 4.6(c). This means that the associated radar image in Fig. 4.4(a) may be free of rain-contamination. In Fig. 4.6(d), the directions in which  $N_\phi$  is less than  $N_T$  are recognized as more affected by rain and data located in these portions are rejected. From Fig. 4.6(d), it may be inferred that the filtered more-rain-affected portions are in the directions of  $0^\circ$ – $191^\circ$  and  $315^\circ$ – $360^\circ$ . Moreover, to quantify the extent of rain contamination for each image, a new rain recognition parameter, the rain rejection percentage (RRP, i.e., the percentage of directions rejected due to rain contamination) is proposed.

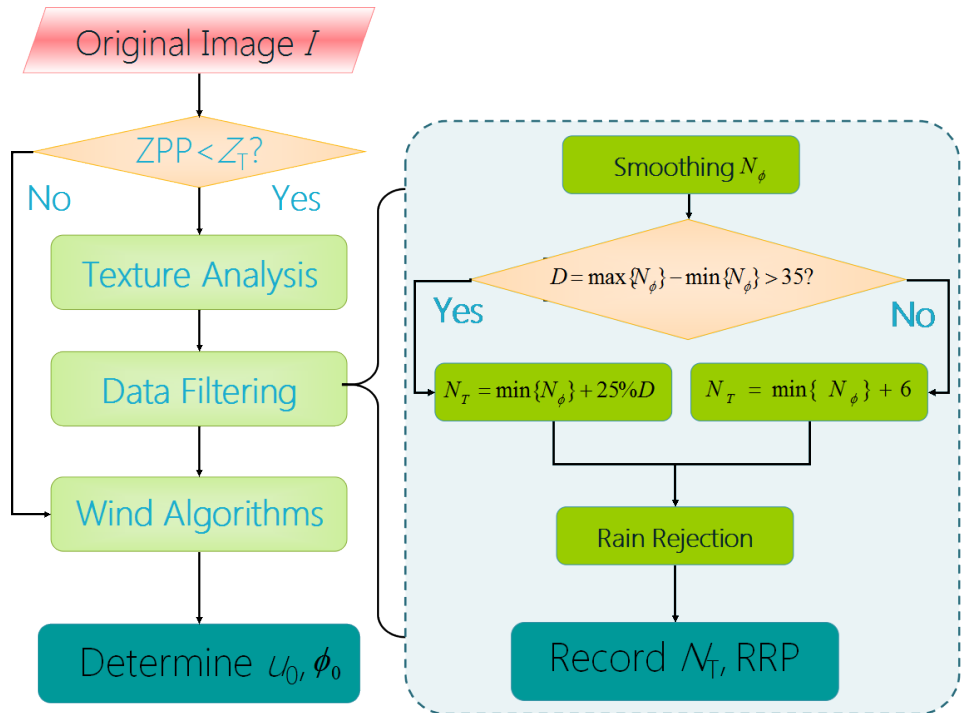


Figure 4.5: Block diagram of rain mitigation.

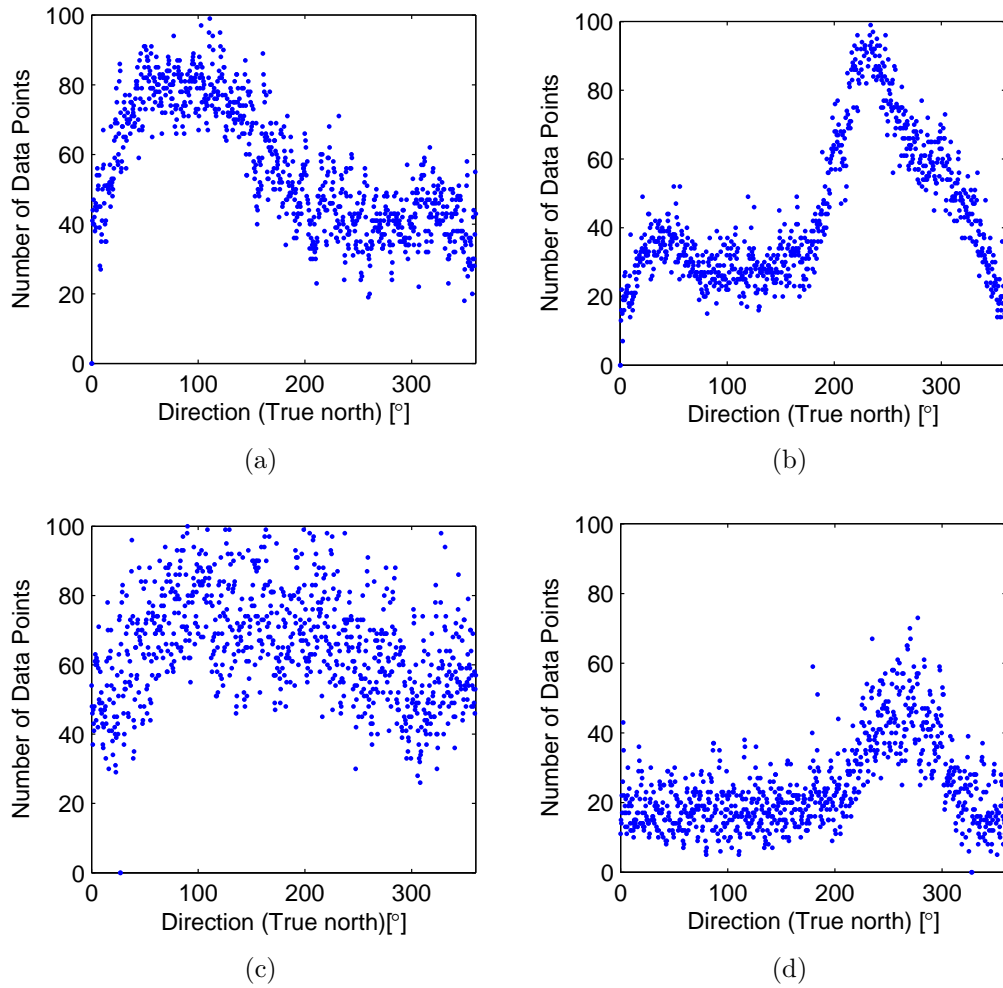


Figure 4.6: Number of data points  $N_\phi$  of: (a) rain-free original image; (b) rain contaminated original image; (c) rain-free texture map; (d) rain-contaminated texture map.

### 4.2.3 Wind Direction

Once the more-rain-affected portions of the radar images are rejected, wind parameters are extracted using both the modified curve-fitting based and ILS-based algorithms. Fig. 4.7 shows the comparison of the results obtained using the curve-fitting-based algorithm with and without rain mitigation. Fig. 4.8 similarly illustrates the results of the ILS-based algorithms. The uniformly bright radar signatures of rain cells can be clearly seen in both the single image and the integrated image, as shown in Figs. 4.7 (a) and 4.8(a). By utilizing the data filtering technique (as described

in Section 4.3.2), the portion less affected by rain can be easily recognized from the texture map (marked by the pink arc in Fig. 4.7(b)). Fig. 4.7(c) shows the corresponding range averaged intensity of the original image (Fig. 4.7(a)). Its harmonic characteristics (as described in Eq. (2.1)) were essentially lost due to the presence of rain and the wind direction error is large. However, after removing the data more-affected by rain, the fitted curve using only the less-affected portions can provide a better result (see Fig. 4.7(d)). The anemometer measured wind direction (see the black bar in Figs. 4.7(a) and (b), 4.8(a) and (b), and the vertical lines in Figs. 4.7 (d) and 4.8(d)) is about  $125^\circ$ . The radar retrieved wind direction using curve-fitting based method with rain mitigation was corrected from  $54^\circ$  to  $110^\circ$ . Similarly, for the

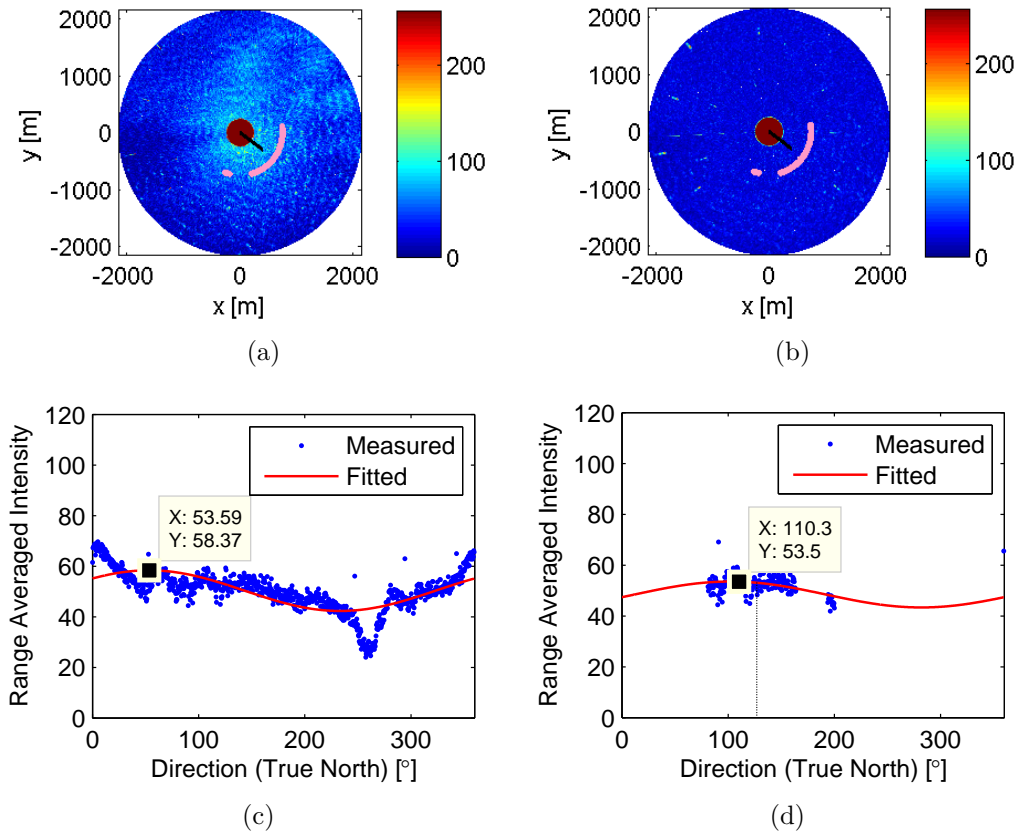


Figure 4.7: Illustration of rain mitigation incorporated curve-fitting based algorithms: (a) the original radar image; (b) the texture map; (c) curve-fitting based method without rain mitigation; (d) curve-fitting based method with rain mitigation.

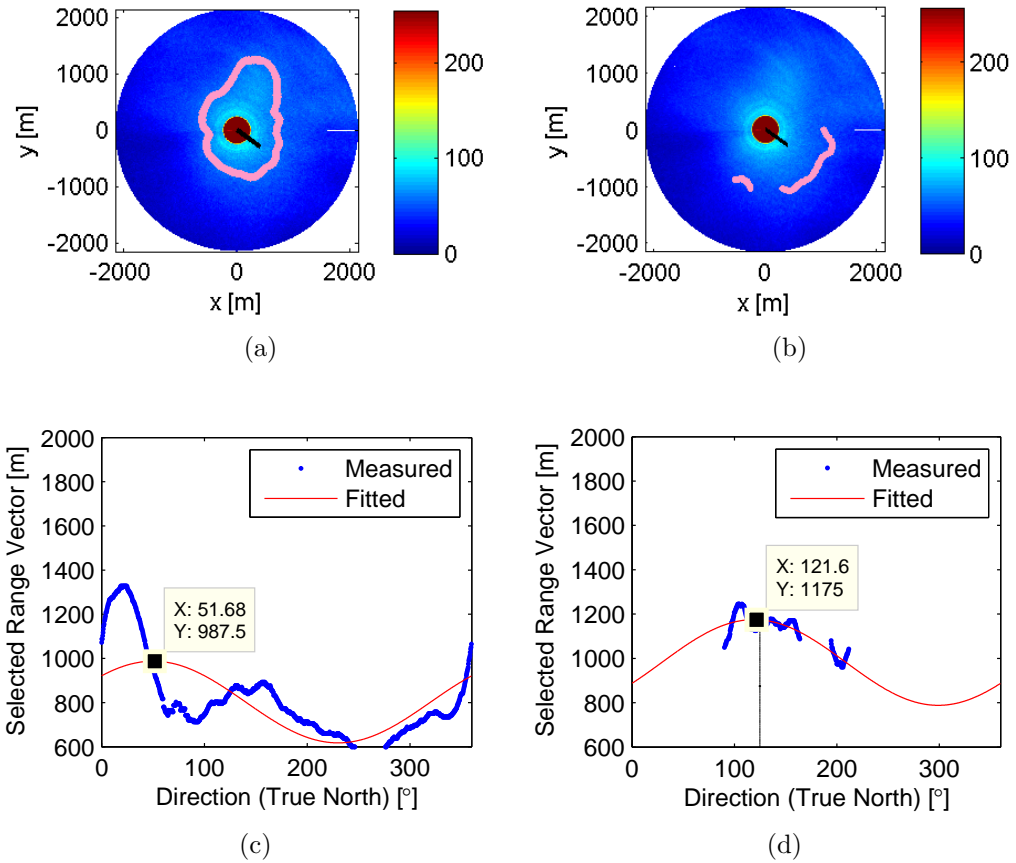


Figure 4.8: Illustration of rain mitigation incorporated ILS based algorithms: (a) ILS without rain mitigation; (b) ILS with rain mitigation; (c) modified ILS-based method without rain mitigation; (d) modified ILS-based method with rain mitigation.

ILS based method, the range distances vector can be improved significantly with rain mitigation (see the Figs. 4.8(c) and (d)). Using the modified ILS based method with rain mitigation, wind direction result has been improved from  $52^\circ$  to  $122^\circ$ .

#### 4.2.4 Wind Speed Model Correction

It was found in Figs. 3.8(b) and 4.3(a) that large wind speed errors occurred for the rain period of 08:00 to 10:00, Nov. 27, due to the inapplicability of the rain-free wind speed models for rain-contaminated data (see Fig. 2.1). Thus, wind speed models for rain-contaminated data should be obtained [59]. Fig. 4.9 shows the comparison of the third-order polynomial models trained using only rain-free data and rain-contaminated data. The corrected models (see Figs. 4.9 (b) and (d)) will be used

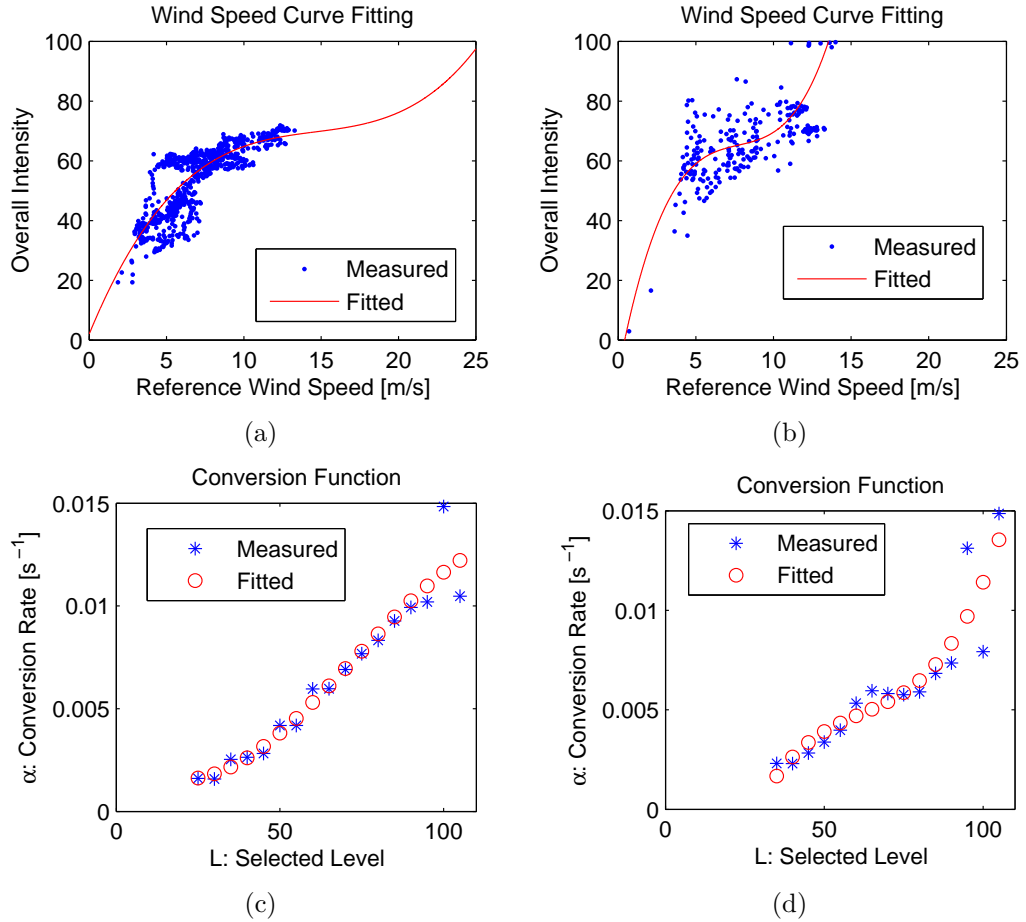


Figure 4.9: Training models: (a) curve-fitting-based wind speed model from rain-free data; (b) curve-fitting-based wind speed model from rain-contaminated data; (c) ILS-based conversion function from rain-free data; (d) ILS-based conversion function from rain-contaminated data.

for the recognized rain-contaminated data to improve the accuracy of wind speed determination.

### 4.3 Results

By utilizing the rain recognition technique proposed in [15] in Dataset 1 (see Table 2.1), 9924 out of 49182 images (i.e. 312 out of 1540 files) were identified as rain cases from the 4-day experiment data. Here, only the wind results from these rain-contaminated images are displayed. The comparison of wind results using the

Table 4.1: Wind speed and direction error statistics from rain-contaminated data

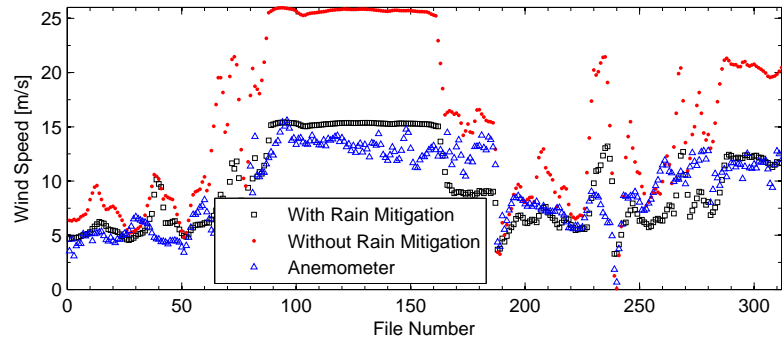
| Algorithm                                       | Wind Direction Error |         | Wind Speed Error |           |
|---|----------------------|---------|------------------|-----------|
|   | Bias [°]             | STD [°] | Bias [m/s]       | STD [m/s] |
| Modified ILS<br>With Rain Mitigation            | 5.3                  | 19.9    | 0.3              | 2.0       |
| Modified ILS<br>Without Rain Mitigation         | 14.7                 | 34.4    | 2.1              | 3.3       |
| Single-curve-fitting<br>With Rain Mitigation    | 4.0                  | 21.5    | 0.2              | 2.4       |
| Single-curve-fitting<br>Without Rain Mitigation | 10.1                 | 28.9    | 6.3              | 5.0       |

modified curve-fitting and ILS based algorithms incorporating rain mitigation are shown in Figs. 4.10 and 4.11, respectively, in which the anemometer data is plotted as ground truth. In practice, a similar 10-minute averaging was applied (if the data is continuous) to both the anemometer and radar wind results before computing the statistical errors shown in Table 4.1. In Figs. 4.10(a) and 4.11(a), wind speeds obtained by utilizing the proposed methods described in Section 4.2 show remarkable improvement over the period from 07:48 to 10:32 on Nov. 27 (i.e., File No. 80 to No. 157), during which continuous rain was identified. With rain mitigation, the mean errors of wind direction and speed obtained for this period using the two improved methods are reduced by  $5.4^\circ$  and  $10.3$  m/s, and  $11.6^\circ$  and  $4.9$  m/s, respectively. Under the low wind speed period from 01:45 to 03:30, Nov. 27 (i.e., File No. 1 to 50), it was found in Fig. 4.10(c) that the RRP is relatively higher (around or above 50%), which reveals that images during this period were more affected by rain. This also agrees with the findings in [57] that the lower the ambient wind speed, the higher is the contrast between the bright pattern and the surroundings. In other words, radar signatures of rain cells may be more distinct when the ambient wind speed is lower. Thus, the rain mitigation technique works effectively during this period. A significant improvement on the wind direction mean error and STD by about  $16.1^\circ$  and  $21.5^\circ$  can be seen during this period (see Fig. 4.11(b)). However, it should be noted that when

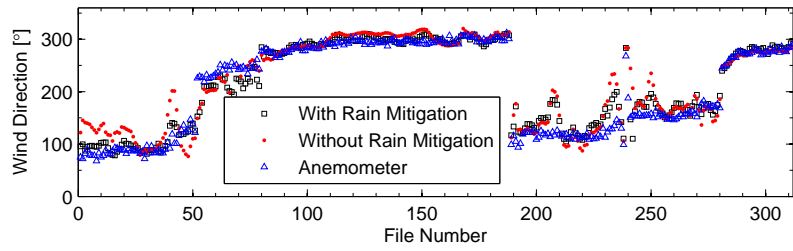
the RRP is too high (i.e., more than 60% of the directions in an image are rejected), reliability of wind direction retrieval using the two algorithms may be reduced (see No.39 to No.43 in Figs. 4.10(b) and 4.11(b)). It was discussed in Section 4.2 that the portions around the downwind direction are relatively more affected by rain. This reveals why the portions around the upwind direction are usually retained after data filtering. Therefore, after rain mitigation, when the curve-fitted ILS is not credible due to over rejection, the maximum of the smoothed range distances vector without curve-fitting (original ILS) may be used for wind direction estimation. It can be also observed from Figs. 4.10(c) and (d) that a high RRP is usually accompanied by an extremely low ZPP. If the ZPP is too low (less than 1%), the wind direction and wind speed results are always worse, especially when ZPP is almost zero.

## 4.4 General Chapter Summary

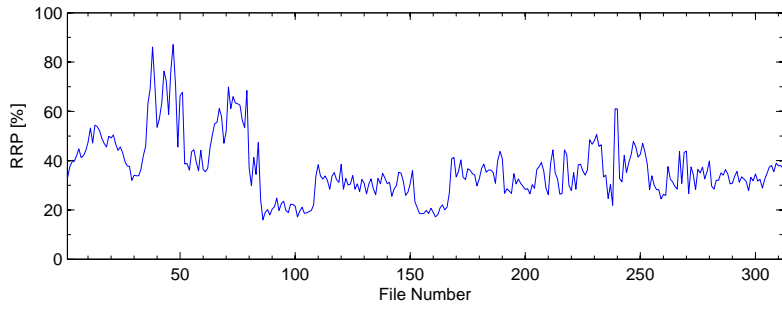
In this chapter, effects of rain on the X-band nautical radar images are elaborated upon and a technique for wind parameter extraction from rain-contaminated images has been proposed. It was illustrated that the rain-contaminated image pixels are more uniformly bright than the wave echoes, and these characteristics can be used to recognize the portions more affected by rain. By removing the data in the directions that are more affected by rain, a texture-analysis-based data filtering process is designed to enhance the performance of two wind algorithms discussed in Chapter 2 and 3. Significant improvements can be seen from the radar-derived wind results using both of these algorithms when rain mitigation is incorporated.



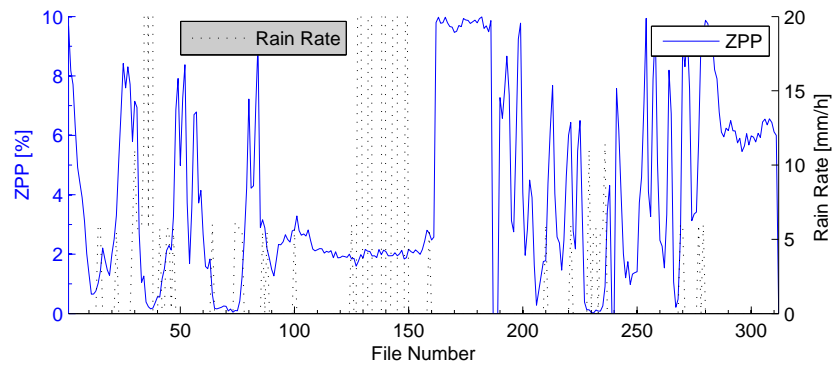
(a)



(b)

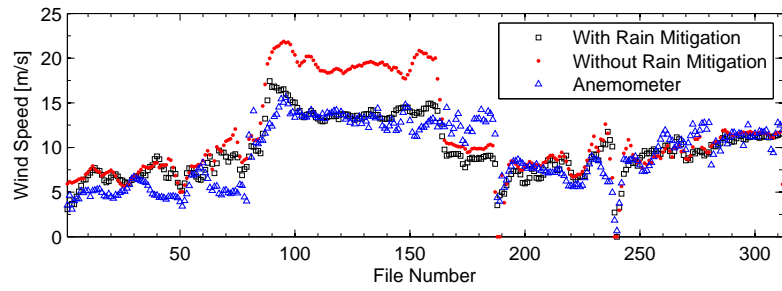


(c)

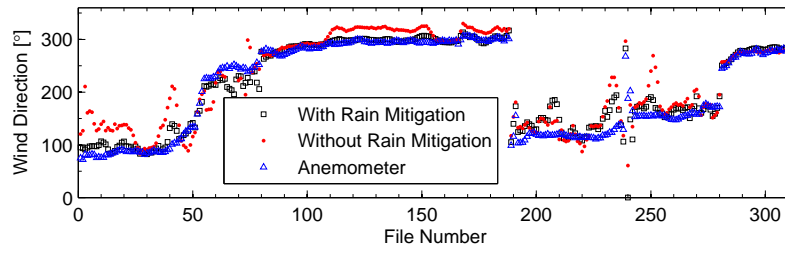


(d)

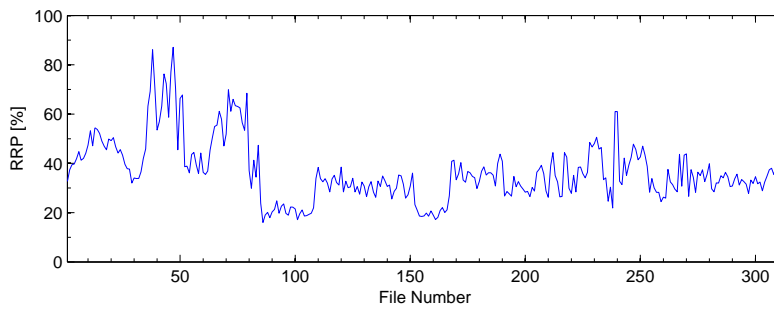
Figure 4.10: Wind results from rain-contaminated data using the curve-fitting based algorithms: (a) wind speed; (b) wind direction; (c) rain rejection percentage; (d) ZPP and precipitation.



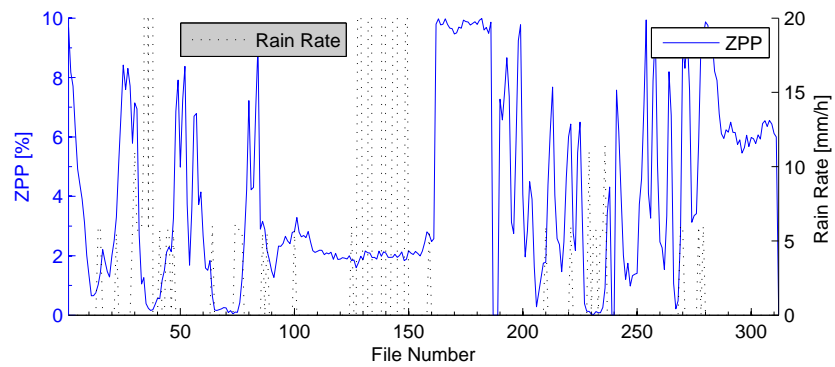
(a)



(b)



(c)



(d)

Figure 4.11: Wind results from rain-contaminated data using the ILS based algorithms: (a) wind speed; (b) wind direction; (c) rain rejection percentage; (d) ZPP and precipitation.

# Chapter 5

## Conclusions

### 5.1 General Synopsis and Significant Results

In this thesis, two modified algorithms for wind retrieval from shipborne X-band nautical radar images and a novel technique for wind estimation from rain-contaminated images are presented and tested using radar and anemometer data collected on the Canadian East Coast.

It was found that reference curve-fitting-based and intensity-level-selection (ILS) based algorithms can perform satisfactorily in normal cases. With the improved dual-curve-fitting algorithm, the wind direction and speed mean difference between the radar and anemometer results can be reduced by about  $5.7^\circ$  and  $0.3$  m/s, respectively, under low sea states. However, the results obtained from single- and dual-curve-fitting are almost the same at higher sea states. It is also shown that the modified ILS method, which involves blockage, island recognition, and curve-fitting, is more robust than the original ILS based method (reference algorithm), since the former can work well even when blockages or islands exist in the radar field of view. Although wind speed results extracted from the modified ILS method are not improved distinctly, the modified ILS method reduces the mean differences and STD of wind direction between the radar and the anemometer results by about  $3^\circ$  and  $4.9^\circ$ , respectively, in Dataset 2.

Moreover, the radar measurements from dual-curve-fitting and the modified ILS agree with each other for most of the data used here, and the mean difference and STD between the anemometer data and the radar results observed using the two methods for wind direction and speed are close. For the data considered in this work, the overall STDs for wind direction and speed are  $6.6^{\circ}$ - $21.2^{\circ}$  and 0.5-2.0 m/s, respectively, which are a little higher than the results (less than  $17.4^{\circ}$  for direction and less than 1.1 m/s for speed) in the open literature (e.g., [12]–[14], [15] and [17]). It should be noted that the temporally-averaged radar-derived wind results also represent spatial average values within the radar coverage, while the temporally-averaged anemometer data represent point measurements at the ship location. This may account for some of the difference between the radar and anemometer results. In addition, correcting the wind speed measurements for the atmospheric stability condition may improve the results [14].

Furthermore, X-band radar signatures of rain cells are analyzed and a technique for mitigation the effects of rain on wind parameter extraction has been proposed. A texture-analysis-based rain mitigation process is incorporated into the above two modified wind algorithms. It was found that radar image intensity is uniformly bright in the presence of rain. By utilizing this property, the portions more affected by rain in an image can be recognized. After removing the data in the directions that are more affected by rain, significant improvements can be achieved in the radar-derived wind results using both algorithms when rain mitigation is incorporated.

## 5.2 Suggestions for Future Work

Several limitations of the methods should be noted. Firstly, modelling of the curve-fitting based approach is not yet sufficiently robust. Building proper models for wind speed retrieval depends on several factors, such as the accuracy of anemometer data. Second, rain recognition was not successful for some datasets. A more intelligent way

to identify and eliminate the effects of rain is required. A threshold in terms of signal-to-noise ratio instead of the grey scale intensity may be used for rain recognition. Third, if the RRP is too high, the rain mitigation technique proposed in Chapter 4 may be unreliable. More data analysis is required to validate whether the more rain-affected portions of radar signatures always occur around the downwind direction.

In the future, investigation of the possibility of retrieving wind direction from the texture map alone could be conducted. Further efforts are ongoing to compare the performance of wind extraction from the horizontally- and vertically-polarized radar data as discussed in [69]. In addition, it may be meaningful to extend the research on the effects of rain in the frequency domain.

# Bibliography

- [1] B. I. Moat, M. J. Yelland, R. W. Pascal, and A. F. Molland., “The effect of ship shape and anemometer location on wind speed measurements obtained from ships,” *in Proc. 4th Int. Conf. on Marine Computational Fluid Dynamics (CFD)*, The Royal Institution of Naval Architects, pp. 133-139, Southampton, UK, Mar. 2005.
- [2] F.T. Ulaby, R.K. Moore and A.K. Fung, *Microwave remote sensing: Active and passive; volume II: Radar remote sensing and surface scattering and emission theory*, Artech House, 1982.
- [3] C. Li, “Sea surface oil slick detection and wind field measurement using global navigation satellite system reflectometry,” *Master thesis, Memorial University of Newfoundland, Engineering and Applied Science*, May 2014.
- [4] B. Lund, “Development and evaluation of new algorithms for the retrieval of wind and internal wave parameters from shipborne marine radar data,” *PhD thesis, University of Miami, Rosenstiel School of Marine and Atmospheric Science*, Nov. 2012.
- [5] “WaMoS II wave and surface current monitoring system operating manual version 4.0.” Internet: [http://www.oceanwaves.org/download/PDF/WaMoSII\\_Manual\\_V4.0.pdf](http://www.oceanwaves.org/download/PDF/WaMoSII_Manual_V4.0.pdf), [May. 2, 2012]

- [6] I. R. Young, W. Rosenthal, and F. Ziemer, "A three-dimensional analysis of marine radar images for the determination of ocean wave directionality and surface currents," *J. Geophys. Res.*, vol. 90, no. C1, pp. 1049-1059, Jan. 1985.
- [7] J. C. Nieto-Borge and C. Guedes-Soares, "Analysis of directional wave fields using X-band navigation radar," *Coastal Eng.*, vol. 40, no. 4, pp. 375-391, Jul. 2000.
- [8] R. Gangeskar, "Ocean current estimated from X-band radar sea surface images," *IEEE Trans. Geosci. Remote Sens.*, vol. 40, no. 4, pp. 783-792, Apr. 2002.
- [9] F. Serafino, C. Lugni, and F. Soldovieri, "A novel strategy for the surface current determination from marine X-band radar data," *IEEE Geosci. Rem. Sens. Lett.*, vol. 7, no. 2, pp. 231-235, Apr. 2010.
- [10] L. Cui, Y. He, H. Shen, and H. Lu, "Measurements of ocean wave and current field using dual polarized X-band radar," *Chinese J. Oceanol. Limnol.*, vol. 28, no. 5, pp. 1021-1028, Sept. 2010.
- [11] W. Huang, E. W. Gill, and J. An, "Iterative least-squares-based wave measurement using X-band nautical radar," *IET Radar Sonar Navig.*, 2014. (in press)
- [12] H. Dankert, J. Horstmann, and W. Rosenthal, "Ocean wind fields retrieved from radar-image sequences," *J. Geophys. Res.: Oceans (1978-2012)*, vol. 108, no. C11, pp. 3352, Nov. 2003.
- [13] H. Dankert, J. Horstmann, and W. Rosenthal, "Wind- and wave-field measurements using marine X-band radar-image sequences," *IEEE J. Oceanic Eng.*, vol. 30, no. 3, pp. 534-542, Jul. 2005.
- [14] H. Dankert and J. Horstmann, "A marine radar wind sensor," *J. Atmos. Oceanic Technol.*, vol. 24, no. 9, pp. 1629-1642, Sept. 2007.

- [15] B. Lund, H. C. Graber, and R. Romeiser, "Wind retrieval from shipborne nautical X-band radar data," *IEEE. Trans. Geosci. Rem. Sens.*, vol. 50, no. 10, pp. 3800-3811, Oct. 2012.
- [16] B. Lund, H. C. Graber, J. Horstmann, and E. Terrill, "Ocean surface wind retrieval from stationary and moving platform marine radar data," in *Proc. IEEE IGARSS*, Munich, Germany, pp. 2790-2793, Jul. 2012.
- [17] R. Vicen-Bueno, J. Horstmann, E. Terril, T. de Paolo, and J. Dannenberg, "Real-time ocean wind vector retrieval from marine radar image sequences acquired at grazing angle," *J. Atmos. Oceanic Technol.*, vol. 30, no. 1, pp. 127-139, Jan. 2013.
- [18] P. S. Bell, "Shallow water bathymetry derived from an analysis of X-band marine radar images of waves," *Coastal Eng.*, vol. 37, no. 3, pp. 513-527, Aug. 1999.
- [19] C. M. Senet, J. Seemann, S. Flampouris, and F. Ziemer, "Determination of bathymetric and current maps by the method DiSC based on the analysis of nautical X-band radar image sequences of the sea surface," *IEEE. Trans. Geosci. Rem. Sens.*, vol. 46, no. 8, pp. 2267-2279, Aug. 2008.
- [20] S. Flampouris, F. Ziemer, and J. Seemann, "Accuracy of bathymetric assessment by locally analyzing radar ocean wave imagery (February 2008)," *IEEE. Trans. Geosci. Rem. Sens.*, vol. 46, no. 10, pp. 2906-2913, Oct. 2008.
- [21] European Wind Energy Association (EWEA), "*Wind energy– the facts: a guide to the technology, economics and future of wind power*," London ; Sterling, VA : Earthscan, 2009.
- [22] Rykaczewski, R. R., and D. M. Checkley, "Influence of ocean winds on the pelagic ecosystem in upwelling regions," in *Proc. Natl. Acad. Sci.*, vol. 105, no. 6, pp. 1965-1970, Feb. 2008.

- [23] D. E. Barrick, "Rough surface scattering based on the specular point theory," *IEEE Trans. Antennas Propag.*, vol. 16, no. 4, pp. 449-454, Jul. 1968.
- [24] D. E. Barrick and W. H. Peake, "A review of scattering from surfaces with different roughness scales," *Radio Sci.*, vol. 3, pp. 865-868, Jan. 1968.
- [25] D. E. Barrick, "Wind dependence of quasi-specular microwave sea scatter," *IEEE Trans. Antennas Propag.*, vol. 22, no. 1, pp. 135-136, Jan. 1974.
- [26] F. G. Bass, I. M. Fuks, A. I. Kalmykov, I. E. Ostrovsky, and A. D. Rosenberg, "Very high frequency radiowave scattering by a disturbed sea surface, Parts I and II: Scattering from an actual sea surface," *IEEE Trans. Antennas Propag.*, vol. 16, no. 5, pp. 554-568, Sept. 1968.
- [27] G. R. Valenzuela, "Theories for the interaction of electromagnetic and oceanic waves - A review," *Bound.-Layer Meteor.*, vol. 13, no. 1-4, pp. 61-85, Jan. 1978.
- [28] G. S. Brown, *Surface Waves and Fluxes; Volume II: Remote Sensing*, "Chapter 10: Quasi-specular scattering from the air-sea interface," pp. 1-39. Kluwer, 1990.
- [29] G. S. Brown, "Guest editorial—Special issue on low-grazing-angle backscatter from rough surfaces," *IEEE Trans. Antennas Propag.*, vol. 46, no. 1, pp. 1-2, Jan. 1998.
- [30] W. L. Bragg, "The diffraction of short electromagnetic waves by a crystal," *in Proc. Cambridge Phil. Soc.*, vol. 17, no. 43, pp. 4, 1913.
- [31] D. D. Crombie, "Doppler spectrum of sea echo at 13.56 Mc./s," *Nature*, vol. 175, no. 4459, pp. 681-682, Apr. 1955.
- [32] J. Wright, "Backscattering from capillary waves with application to sea clutter," *IEEE Trans. Antennas Propag.*, vol. 14, no. 6, pp. 749-754, Nov. 1966.

- [33] J. Wright, "A new model for sea clutter," *IEEE Trans. Antennas Propag.*, vol. 16, no. 2, pp. 217-223, Mar. 1968.
- [34] W. Plant, *Surface Waves and Fluxes; Volume II: Remote Sensing*, "Chapter 11: Bragg scattering of electromagnetic waves from the air/sea interface," pp. 41-108. Kluwer, 1990.
- [35] L. B. Wetzel, *Surface Waves and Fluxes; Volume II: Remote Sensing*, "Chapter 12: Electromagnetic scattering from the sea at low grazing angles," pp. 109-171. Kluwer, 1990.
- [36] W. J. Plant and D. L. Schuler, "Remote sensing of the sea surface using one- and two-frequency microwave techniques," *Radio Sci.*, vol. 15, no. 3, pp. 605-615, May-June 1980.
- [37] W. R. Alpers and K. Hasselmann, "The two-frequency microwave technique for measuring ocean-wave spectra from an airplane or satellite," *Bound.-Lay. Meteorol.*, vol. 13, no. 3, pp. 215-230, Jan. 1978.
- [38] W. R. Alpers, D. B. Ross, and C. L. Rufenach, "On the detectability of ocean surface waves by real and synthetic aperture radar," *J. Geophys. Res.*, vol. 86, no. C7, pp. 6481-6498, Jul. 1981.
- [39] B. G. Smith, "Geometrical shadowing of a random rough surface," *IEEE Trans. Antennas Propag.*, vol. 15, no. 5, pp. 668-671, Sept. 1967.
- [40] D. E. Barrick, "Near-grazing illumination and shadowing of rough surfaces," *Radio Sci.*, vol. 30, no. 3, pp. 563-580, 1995.
- [41] I. S. Robinson, "Measuring the Oceans from Space - The principles and methods of satellite oceanography," *Springer Berlin/Heidelberg/New York*, 2004.

- [42] G. Watson and I. S. Robinson, "A study of internal wave propagation in the Strait of Gibraltar using shore-based marine radar images," *J. Phys. Oceanogr.*, vol. 20, no. 3, pp. 374-395, Mar. 1990.
- [43] J. Dittmer, "Use of marine radars for real time wave field survey and speeding up transmission/processing," in *Proc. WMO/IOC Workshop on Operational Ocean Monitoring Using Surface Based Radars*, vol. 32, pp. 133-137, Geneva, Switzerland, Mar. 1995.
- [44] A. Chaudhry and R. Moore, "Tower-based backscatter measurements of the sea," *IEEE J. Oceanic Eng.*, vol. 9, no. 5, pp. 309-316, Dec. 1984.
- [45] P. H. Y. Lee, J. D. Barter, K. L. Beach, C. L. Hindman, B. M. Lake, H. Rungaldier, J. C. Shelton, A. B. Williams, R. Yee, and H. C. Yuen, "X-band microwave backscattering from ocean waves," *IEEE J. Geophys. Res.*, vol. 100, no. C2, pp. 2591-2611, Feb. 1995.
- [46] P. H. .Y. Lee, J. D. Barter, E. Caponi, M. Caponi, C. L. Hindman, B. M. Lake, and H. Rungaldier, "Wind-speed dependence of small-grazing-angle microwave backscatter from sea surfaces," *IEEE Trans. Antennas Propag.*, vol. 44, no. 3, pp. 333-340, Mar. 1996.
- [47] D. B. Trizna and D. Carlson, "Studies of dual polarized low grazing angle radar sea scatter in nearshore regions," *IEEE Trans. Geosci. Remote Sens.*, vol. 34, no. 3, pp. 747-757, May 1996.
- [48] D. B. Trizna, "A model for Brewster angle damping and multipath effects on the microwave radar sea echo at low grazing angles," *IEEE Trans. Geosci. Rem. Sens.*, vol. 35, no. 5, pp. 1232-1244, Sept. 1997.
- [49] H. Hatten, F. Ziemer, J. Seemann, and J. Nieto-Borge, "Correlation between the spectral background noise of a nautical radar and the wind vector," in *Proc.*

- 17th Int. Conf. Offshore Mechanics and Arctic Eng. (OMAE)*, Lisbon, Portugal, 1998.
- [50] H. Hatten, F. Ziemer, J. Seemann, and J. Nieto-Borge, "Azimuthal dependence of the radar cross section and the spectral background noise of a nautical radar at grazing incidence," in *Proc. Geosci. Rem. Sens. Symp. (IGARSS)*, Seattle, USA., Jul. 1998.
- [51] P. Izquierdo and C. G. Soares, "Analysis of sea waves and wind from X-band radar," *Ocean. Eng.*, vol. 32, no. 11-12, pp. 1404-1419, Aug. 2005.
- [52] W. C. Keller, W. J. Plant, R. A. Petitt, Jr, and E. A. Terray, "Microwave backscatter from the sea: Modulation of received power and Doppler bandwidth by long waves," *J. Geophys. Res.*, vol. 99, no. C5, pp. 9751-9766, May 1994.
- [53] J. R. Garratt, *The Atmospheric Boundary Layer*, Cambridge, U.K.: Cambridge Univ. Press, 1992.
- [54] C. Melsheimer, W. Alpers, and M. Gade, "Investigation of multifrequency/multipolarization radar signatures of rain cells over the ocean using SIRC/XSAR data," *J. Geophys. Res.: Oceans (1978-2012)*, vol. 103, no. C9, pp. 18867-18884, Aug. 1998.
- [55] J. Tournadre and Y. Quilfen, "Impact of rain cell on scatterometer data: 1. Theory and modeling," *J. Geophys. Res.*, vol. 108, no. C7, pp. 18-1-18-14, Jul. 2003.
- [56] R. F. Contreras and W. J. Plant, "Surface effect of rain on microwave backscatter from the ocean: Measurements and modeling," *J. Geophys. Res.*, vol. 111, no. C08, pp. C08019, Aug. 2006.

- [57] W. Alpers and C. Melsheimer, "SAR marine users manual-chapter 17- Rainfall." Internet: [http://www.sarusersmanual.com/ManualPDF/NOAASARManual\\_CH17\\_pg355-372.pdf](http://www.sarusersmanual.com/ManualPDF/NOAASARManual_CH17_pg355-372.pdf), [Jun. 1, 2013]
- [58] Y. Liu, W. Huang, and E. W. Gill, "Analysis of the effects of rain on surface wind retrieval from X-band marine radar images," in *Proc. IEEE OCEANS*, St. John's, Canada, 2014 (accepted).
- [59] W. Huang, Y. Liu, E. W. Gill "Texture-analysis-incorporated wind parameters extraction from rain-contaminated X-band nautical radar images," *IEEE*, 2014 (under revision).
- [60] C. Nie and D. G. Long "A C-band wind/rain backscatter model," *IEEE. Trans. Geosci. Rem. Sens.*, vol.45, no.3, pp.621-631, Mar. 2007.
- [61] M. K. Jang and C. S. Cho "Target detection of marine radars using matrix bank filters," in *Proc. Asia-Pacific Microwave Conf.*, pp. 1046-1048, Kaohsiung, Taiwan, Dec. 2012.
- [62] J. J. Gourley, P. Tabary, and J. P. Du Chatelet "A fuzzy logic algorithm for the separation of precipitating from nonprecipitating echoes using polarimetric radar observations," *J. Atmos. Oceanic Technol*, vol.24, no.8, pp. 1439-1451, Aug. 2007.
- [63] W. J. Plant, "A two-scale model of short wind-generated waves and scatterometry," *J. Geophys. Res.*, vol. 91, no. C9, pp. 10735-10759, Sept. 1986.
- [64] H. Hatten, J. Seemann, J. Horstmann, and F. Ziemer, "Azimuthal dependence of the radar cross section and the spectral background noise of a nautical radar at grazing incidence," in *Proc. IEEE IGARSS*, vol. 5, pp. 2490-2492, Seattle, USA, Jul. 1998.

- [65] D. C. Stredulinsky and E. M. Thornhill “Ship motion and wave radar data fusion for shipboard wave measurement,” *J. Ship Res.*, vol. 55, no. 2, pp. 73-85, Jun. 2011.
- [66] N. Braun, M. Gade, and P. A. Lange, “Radar backscattering measurements of artificial rain impinging on a water surface at different wind speeds,” in *Proc. IEEE IGARSS*, vol. 1, pp. 200-202, Hamburg, Germany, Jul. 1999.
- [67] Y. Liu, W. Huang, and E. W. Gill, “Intensity-level-selection-based wind retrieval from shipborne nautical X-band radar data,” in *Proc. IEEE IGARSS*, Québec, Canada, Jul. 2014.
- [68] Y. Liu, W. Huang, E. W. Gill, D. Peters, and R. Vicen-Bueno, “Comparison of algorithms for wind parameters extraction from X-band shipborne marine radar images,” *IEEE J. Sel. Topics Appl. Earth Observ. Remote Sens.*, 2014. (accepted)
- [69] W. Huang, E. W. Gill, “Surface current measurement under low sea state using dual polarized X-band nautical radar,” *IEEE J. Sel. Topics Appl. Earth Observ. Rem. Sens.*, vol. 5, no. 6, pp. 1868-1873, Dec. 2012.